Experimental and numerical multiscale testing of CFRP bonded stepped repairs

Jean-Baptiste Orsatelli, Eric Paroissien, Frédéric Lachaud, Sébastien Schwartz, Nathalie Barrière

Thin–Walled Structures 208 (2025) 112764

Contents lists available at ScienceDirect

Thin-Walled Structures

journal homepage: www.elsevier.com/locate/tws

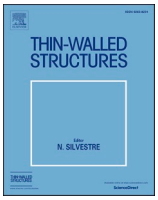

Full length article

Experimental and numerical multiscale testing of CFRP bonded stepped repairs

Jean-Baptiste Orsatelli [a,b,*], Eric Paroissien [a], Frédéric Lachaud [a], Sébastien Schwartz [a], Nathalie Barrière [b]

[a] Institut Clément Ader (ICA), Université de Toulouse, ISAE-SUPAERO, INSA, IMT MINES ALBI, UTIII, CNRS, 3 Rue Caroline Aigle, 31400 Toulouse, France
[b] DGA Techniques Aéronautiques, 47 rue Saint-Jean, Balma 31131, France

ARTICLE INFO

Keywords:
Bonding
Composite
Repair
Failure
Damage

ABSTRACT

Bonded stepped repairs to aircraft composite structures offer many advantages, such as a smooth aerodynamic surface, high strength, and low mass addition. However, their design remains challenging due to the varying stiffness along the bondline in a thin laminate. This study investigates, numerically and experimentally, to what extent an "equivalent" stepped joint can be used to design a stepped repaired panel. In the proposed case, failure is driven by laminate fracture instead of patch disbonding. Tension tests on stepped repairs at the scale of coupons and panels were carried out in 11 different configurations. Specimens were obtained by hot-bonding as it would be done to perform in-situ repairs. Finite element modelling was performed with cohesive zone modelling to account for disbonding and delamination, and continuum damage mechanics to simulate composite failure. This multiscale experimental study showed that stepped repaired coupons have a similar behaviour to repaired panels in terms of damage mechanisms, failure onset location, and tensile strength. It supports the idea to use coupons instead of whole panels to carry out experimental testing of stepped repairs. A good agreement with 2D and 3D numerical simulations was also found. They predicted accurately the strength of the repairs and highlighted a failure location compatible with the experimental results. As a conclusion, an equivalent stepped joint can be representative for the strength of a stepped repaired panel, including when failure occurs inside the laminates.

1. Introduction

The use of composite materials in aeronautical structures has substantially risen over the last decades thanks to their attractive performances [1]. However, these materials are susceptible to damage during their operational lifespan, requiring intervention to restore the original integrity of the structure. Carbon fibre reinforced polymers (CFRP) materials are indeed vulnerable to out-of-plane loading, such as impacts [2], which may occur due to low-speed impacts, such as tool drop or ground collision, or high speed impacts such bird strike. Low velocity impacts can cause delamination between composite plies and development of cracks at the interface between fibres and matrix, which leads to a dramatic decrease of the compressive strength of the impacted composite structure with a barely visible impact damage. The ability to repair a damaged composite structure is therefore a major concern for economic and operational reasons. Several types of repairs can be performed on composite structures: mechanically fastened repairs, bonded repairs or hybrid repairs using both bolts and adhesive bonding. Among those repair types, bonded flush repairs draw a lot of attention as they allow keeping a smooth external surface while providing increased joint strength compared to doubler repairs [3]. By avoiding the use of bolts, they bring two additional benefits: no subsequent mass addition to the original structure, and no need to drill holes in it. The two most common types of flush repairs are scarf repairs, featuring adherends smoothly machined in a scarf shape, and stepped repairs, featuring adherends machined in a stepped shape. Even though these repair types come with many advantages, they are challenging to perform [4] because they require precise machining of the parent structure. Their design is also especially difficult, as the design of structural bonded joints is itself challenging, and there is no current standard existing to do so. Moreover, flush repairs are a particularly complex type of bonded joints, with plies drop-off involving a stiffness variation of the adherends along the bondline.

Multiple modelling approaches dedicated to scarf and stepped joints

* Corresponding author.
E-mail address: jean-baptiste.orsatelli@isae-supaero.fr (J.-B. Orsatelli).

https://doi.org/10.1016/j.tws.2024.112764
Received 16 July 2024; Received in revised form 8 November 2024; Accepted 26 November 2024
Available online 27 November 2024

design have been explored. It began with early analytical models [5] adapted directly from the shear-lag theory [6], before evolving towards semi-analytical models to introduce non-linear behaviour of the adhesive material [7]. In the recent years, the standard shifted towards the use of finite element (FE) modelling. Different modelling approaches were proposed, with two-dimensional (2D) [8,9] and three-dimensional models (3D) [10,11], associated with meshing strategies involving shell [12,13] or brick elements [14,15]. Among the various models that have been proposed, a distinction can be made between those relying on a failure criterion to predict the strength of a flush repair, such as maximum stress, average stress [16] or strain-based criterion [17], and those modelling damage initiation and evolution. The latter is performed thanks to cohesive zone modelling (CZM) [18] and continuum damage mechanics (CDM) [19] based on the fracture energy of the adhesive material and composite laminates. However, high-fidelity simulations using 3D FE with CZM and CDM are very computation intensive. New studies proposing improved semi-analytical modelling of stepped joints [20] were released to match the need for faster tools to design flush repairs. To go further, a review that investigates the different modelling approaches and their agreement with experimental testing was proposed [21].

Among the studies on flush repairs, there are two scales of modelling and testing usually proposed: full scale repaired panel (usually about 300 mm wide) and the "equivalent" repaired coupon (usually about 20 mm wide). Because of the complexity of experimentally testing full-scale repaired panels, only rare studies performed such work [22–26], while most of the literature is focused on studying scarf and stepped joints, at the scale of a coupon. The problem is the same for numerical modelling. This is why many studies are focused on modelling a scarf or stepped joint, which is more convenient than a full-scale repaired panel. This approach comes with the hypothesis that the behaviour of a flush-repaired panel is driven by the behaviour of its most loaded section, which can be described as its *equivalent joint*. This hypothesis is a matter of discussion in the literature thanks to numerical investigation [27,28]. There is an agreement on the fact that the stress state in an equivalent joint is very close to the one in the highest loaded section of a flush repair [29]. Moreover, Tashi and Abedian [30] confirmed by FE modelling that the stress concentration factor in the most loaded section of a 3D scarf repair is close to the one in 2D scarf joints. Their results were consolidated by another numerical study on stepped repairs [31], showing that the load-carrying capacity of the bondline of a 3D stepped-repaired panel under tension loading can be approximated by a 2D model. These studies tend to confirm the hypothesis than the equivalent joint is representative for the behaviour of a full-scale repair, but there are mainly focused of the behaviour of the adhesive layer between the parent plate and the repair patch. Beyond static strength of repairs, it can be mentioned that recent publications are aimed towards residual strength of composite bonded repairs after impact damage [32,33]. Compressive behaviour of bonded composite repairs is also gaining more attention thanks to recent work [34,35,36].

There is still work to be done to pursue the discussion on the equivalent joint given that (i) there is no experimental study that tested stepped repaired panels and their equivalent coupons, (ii) there is no comparison between 2D and 3D FEM models of stepped repairs with CFRP progressive damage modelling, as [30] and [31] used a linear-elastic behaviour of the laminates, and (iii) papers often study bondline failure of the laminates [37] experimentally and numerically, but rarely deal with repairs configuration where failure happens by neat laminate failure, even though the latter is what a repair should aim for. This paper intends to fill those gaps by providing experimental multi-scale testing of stepped repairs, and FE modelling in 2D and 3D by improving the models studied in [31] through the addition of CFRP damage modelling and delamination between plies. It intends to actually study to what extent a stepped joint can be representation for the behaviour of a stepped repaired panels. FE modelling in 2D and 3D is performed to achieve a numerical comparison of the behaviour of panels and equivalent joints and provide a simplified modelling framework for stepped repairs. The numerical part of this work is supported by the experimental data obtained from experimental tension tests.

This work is focused on stepped repairs rather than scarf repairs, because industrial in-situ repairs tend to be closer to a stepped configuration due to plies drop-off [38]. Hence, three different types of specimens under tension loading are studied in this paper (Fig. 1). Thereafter, full scale stepped repaired panels will be referred as *repaired panels*, and their equivalent joints at the scale of a coupon will be referred as *through repaired coupons* and *non-trough repaired coupons,* depending on the damage depth. Coupons and panels refers to the two different scales of specimen considered in the proposed multi-scale study. Multiple patch stacking sequences and damage depths were also considered to investigate the effect of those design parameters and the robustness of the FE models. Results are discussed in terms of damage onset location, failure scenario and repairs strength to compare the different scales of experimental and numerical testing.

2. Experimental work

2.1. Materials used

All specimens were manufactured using Hexcel M18-1/43/G939 carbon epoxy prepreg (referred as G939/M18 in this paper) as the parent material. It is meant to be representative for the structure to be repaired. The G939 is a balanced carbon fabric with a 4H satin weave and a nominal ply thickness of 0.24 mm. The M18 is a thermosetting epoxy matrix that cures at 180°C. This material is typically used in helicopter structures, as a monolithic material or in sandwich structures. Repairs were performed using G939 dry carbon fabric and Hexcel Hexbond 312-L epoxy film adhesive. The latter is a high performance unsupported adhesive film, supplied at a nominal thickness of 0.1 mm and an areal weight of 150 g/m^2. It has a nominal curing temperature of 120°C, making it suitable to perform hot bonding on G939/M18 without degrading the M18 matrix. Repair patches were manufactured by wet-layup of G939 fabric associated with Hexbond 312-L, creating a G939/Hexbond 312-L laminate, and co-bonded onto the parent structures, i.e. the patch is simultaneously cured and bonded onto initial structure. Therefore, the specimens of this study are in the end made of three different materials: G939/M18 for the parent plates, G939/Hexbond-312L for the repair patch, and Hexbond 312-L at the interface between the two latter. The materials properties used for numerical simulations are presented in Section 3, Tables 2 and Table 3, along with the characterisation tests that were performed.

2.2. Testing matrix

The baseline configuration chosen for this study is a stepped repair loaded under tension, with an initial damage size of 30 mm. As G939 is a balanced woven fabric, plies orientations are referred as (0/90) and (+45/-45), ignoring the small variations of properties between the warp and weft direction. An 8-plies-quasi-isotropic stacking sequence of $[(45/\text{-}45), (0/90)]_{2s}$, with a nominal laminate thickness of 1.92 mm, was chosen for the parent structure. A test matrix with four parameters, being the scale of specimen, repair depth, repair layup and step length, was proposed. Two different scales of specimens were tested: repaired coupons, with a width of 20 mm and out-of-overlap length of 50 mm (Fig. 1), and repaired panels, with a width of 300 mm and a length of 450 mm. Two repair depths were considered, including repairs with a depth 4 plies depth out of 8 total plies referred as non-through repairs (NT), and repairs of 8 plies depth out of 8, referred as through-repairs (T). In each configuration, repairs steps were one-ply-deep, i.e. 0.24 mm. Three different step lengths of 4, 8 and 12 mm were tested, resulting in step depth to step length ratios of 1:17, 1:33 and 1:50. It covers the typical step ratio used to perform repairs. Three types of repair patch layup were tested, with matching layup, matching layup

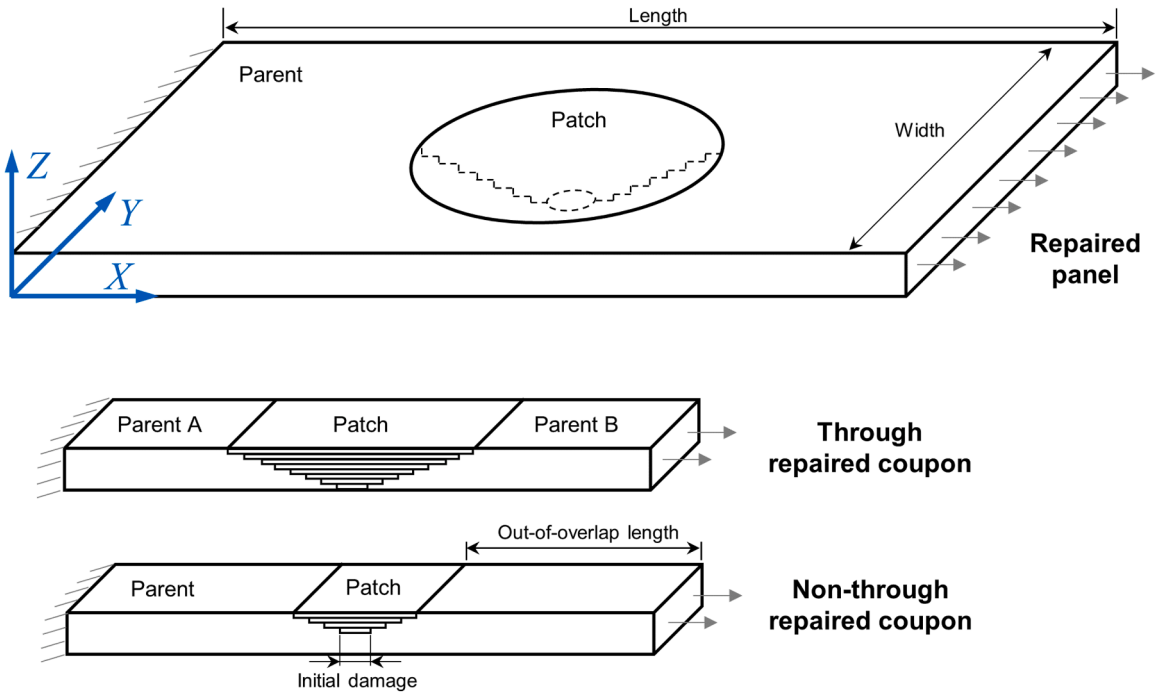

Fig. 1. Types of specimens studied, axis system and loading applied. Adapted from [31].

with an additional 0° overply, or overlapping layup with a 45° overply (Fig. 2). The idea of the overlapping layup is that each repair ply overlaps a parent ply with the same orientation. It is often mentioned as the reference technique to achieve optimal repair performance because each repair ply is bonded to a parent ply with the same orientation [38,39]. The bottom ply, also known as "filler ply", is oriented at 45° to ensure that the stiffness of the patch is close to the stiffness of the parent laminate. On the other hand, the idea of the matching layup is to restore the parent laminate with its original plies orientations. A numbering of step ends is provided in Fig. 2, starting at #0 at the first ply of the parent patch so that it remains applicable no matter the chosen configuration.

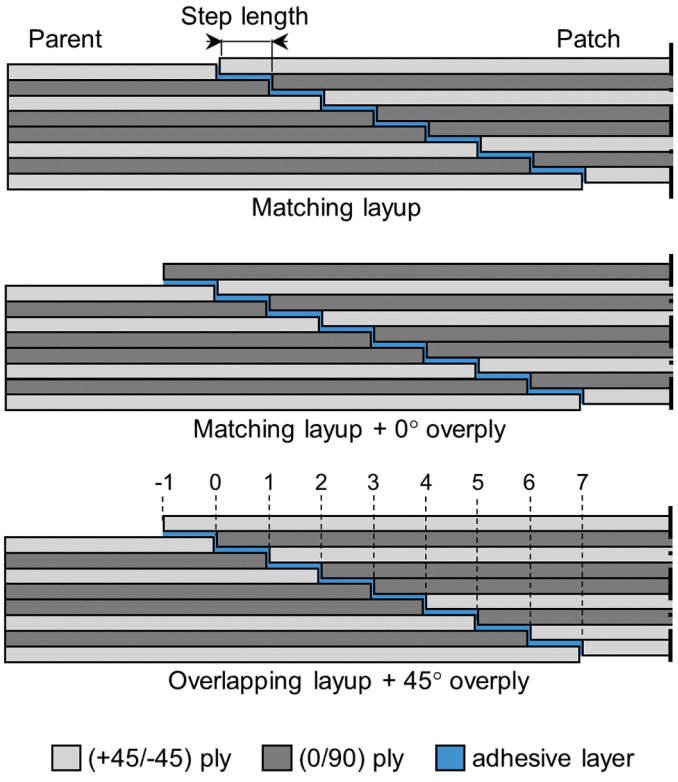

Fig. 2. Tested layups of the repair patch. A numbering of the step ends is also provided. Adapted from [31].

With two parameters taking two values, and the two other taking three values, up to 36 configurations could be tested. The testing matrix was reduced to 11 different configurations (Table 1) by testing the effect of damage depth only on repaired coupons and the effect of patch layup only on through repaired coupons. Repaired panels were tested under tension by sets of three specimens, and repaired coupons by sets of five specimens. In addition, tension tests on G939/M18 coupons with a $[(45/\text{-}45), (0/90)]_{2s}$ layup and a width of 20 mm were carried out to measure the strength of the parent material, so that it can be used to evaluate the repairs strength recovery rate.

2.3. Specimen manufacturing

The general steps followed to obtain the specimens were: (i) curing a parent plate, (ii) machining the edges of the parent plate; (iii) machining the stepped shape; (iv) co-bonding the repair patch; (v) sampling the coupons (coupons only). Each stepped-repaired panel specimen was obtained from a different parent plate (Fig. 3), while each set of non-through repaired coupons were manufactured using a single parent

Table 1
Specimen testing matrix.

Name	Scale	Repair depth	Repair layup	Step length (mm)
C-NT-4M	Coupon	4 plies (NT)	Matching	4
C-NT-8M				8
C-NT-12M				12
C-T-4M	Coupon	8 plies (T)	Matching	4
C-T-8M				8
C-T-12M				12
P-T-4M	Panel	8 plies (T)	Matching	4
P-T-8M				8
P-T-12M				12
C-T-8O	Coupon	8 plies (T)	Overlapping + 45°	8
C-T-8M*	Coupon	8 plies (T)	Matching + 0°	8

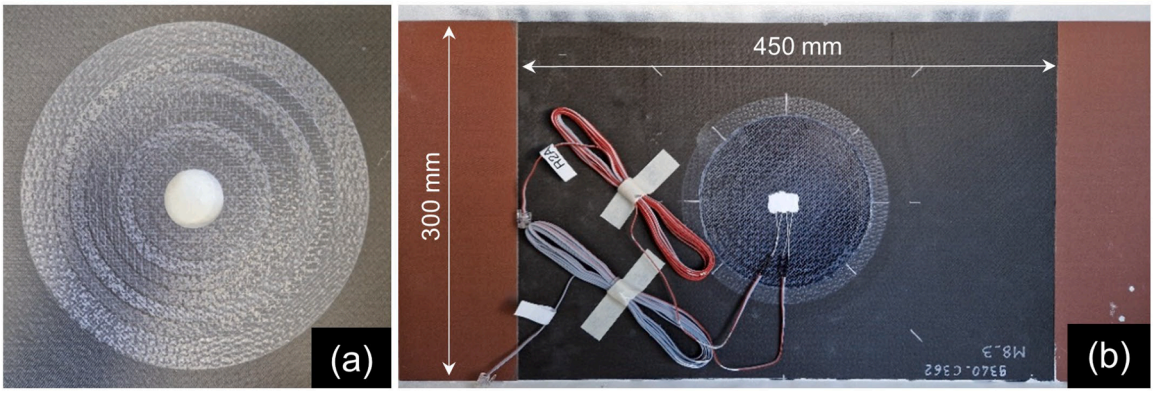

Fig. 3. Stepped repaired panel specimen example. (a) Close-up view of the stepped shape after water jet abrasion machining. (b) Global view of the panel after performing the repair and adding the strain gauges.

plate (Fig. 4). This plate was repaired with rectangular steps before cutting a set of five coupons from this plate in the end. Through-repaired coupons were manufactured in the same way except two parent plates were co-bonded together with the repair patch to obtain a through repair configuration. Each step of the repair process is detailed hereafter.

Parent plates in G939/M18 were hand laid up and cured in an autoclave during 2 hours at 180 °C as recommended by the supplier. Then, to obtain straight parallel edges, the parent plates were machined with a computer numerical control (CNC) diamond wheel for the coupons, CNC milling for the panels. Once parent plates were produced, the stepped shapes were obtained on those plates by abrasive water-jet milling. This was done by the company BAYAB Industries who developed this process [39]. It allows machining automatically one-ply-deep steps by removing parent material with a high-degree of precision, using a water jet filled with abrasive particles. Rectangular steps were machined onto plates destined to make repaired coupon specimens, and circular steps onto plates destined to make repaired plates specimens.

Once the stepped shapes were machined, a degreasing product was applied on the surface before deposing the repairs plies. Each repair ply was made of one layer of Hexbond 312-L film associated with a ply of dry G939 carbon fabric. The two components were first compacted together under vacuum so that they stick together. Then, repair plies were then hand-cut at the right dimensions and applied onto the parent plates. They were aligned using a template to match as close as possible the steps machined on the parent plates. Hand positioning of repair plies with a 4 mm step length is a particularly challenging task. Even a small misalignment of the repair plies, of about 1 mm, is likely to provoke high strength loss of the repair. Co-bonding of the repair patch was done using an ANITA NG9201 mobile repair console to be representative for a real repair. This equipment, developed by GMI AERO, is a portative hot-bonder destined to perform on-field repairs to composite structures. It comes with a heating blanket that is laid up onto the plate to be cured, thermocouples to control the curing temperature, and a vacuum pump (Fig. 5). The curing cycle used for co-bonding last 1h at 110°C with a previous hold at 70°C to let the adhesive material viscosity decrease, in

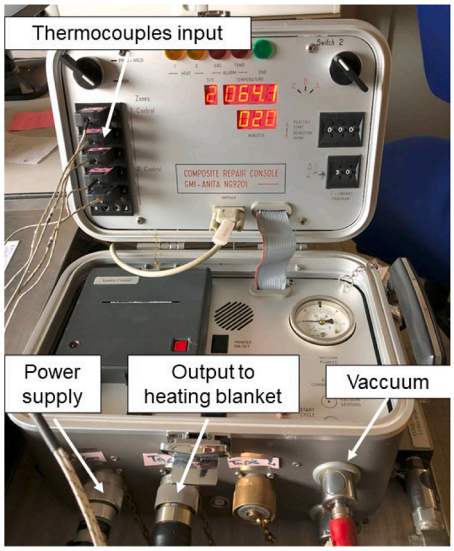

Fig. 5. ANITA repair console.

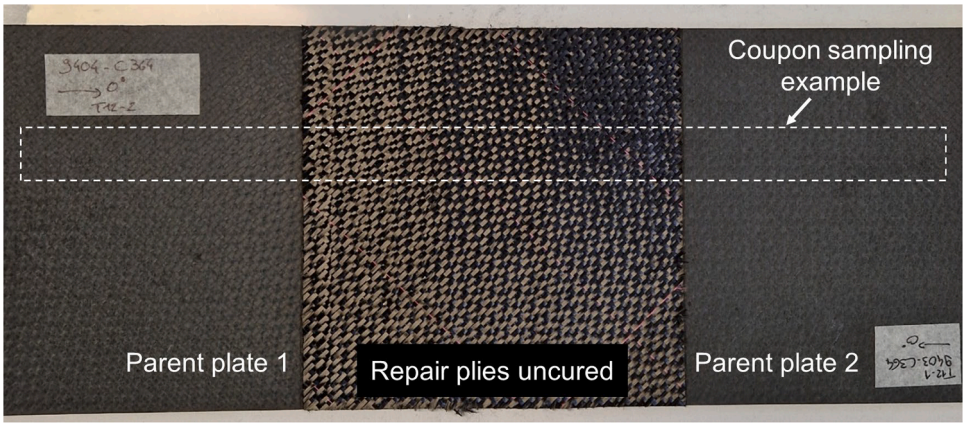

Fig. 4. Through repaired coupons manufacturing process, after added repair plies and before curing. The direction of coupon sampling is also provided.

order it to penetrate the dry fabric. After cooling down the repairs were finished. Repaired coupons required an additional machining step to cut them from the plates by CNC diamond wheel milling.

2.4. Tension testing setup

Repaired coupons were tested using a hydraulic machine, equipped with hydraulic jaws. Specimens hand-aligned with a steel bracket, so that they are parallel to the load axis, and then clamped inside the jaws. The loading was applied at a speed of 1 mm/min until failure of the specimens.

Repaired panels were instrumented before testing with two strain gauges facing each other at the centre of the repair. Panels were spray painted to create a speckle pattern suitable to perform digital image correlation (DIC) during the tests, using a ZEISS ARAMIS-SRX DIC system with a 550 × 400 mm measure volume. The elongation of the specimens was computed using a virtual extensometer of 250 mm gauge length centred on the specimen and oriented in the direction of the load. It includes the entire repaired area between the ends of the extensometer, as the maximum diameter of the repairs tested is 198 mm for P-T-12M specimens (Fig. 6). It was not possible to create a longer DIC extensometer because a part of the specimens was hidden by the jaws. The elongation of the repaired coupons was also measured by DIC, using a virtual extensometer with a base length of 125 mm and one end positioned in the middle of the specimen.

Panels were tested on a testing machine of 3000 kN capacity (Fig. 7) due to the need of large jaws to fit in the 300 mm wide specimen. The applied load was monitored using a 1000 kN measure range. Specimens were clamped inside the hydraulic jaws with a pressure of 120 bar to prevent any sliding during the tension tests. The loading was applied at constant displacement rate of 1 mm/min until failure of the specimens.

3. Finite element modelling

Two types of FE models for stepped repairs were developed using the Abaqus software: a two-dimensional generalized plane strain (2D GPS) model for coupons, and a three-dimensional model for panels (3D Panel). These models are improved versions of the ones presented in [31], by adding progressive damage modelling in the behaviour of the composite adherends and delamination between composite plies in both the 2D GPS and 3D model.

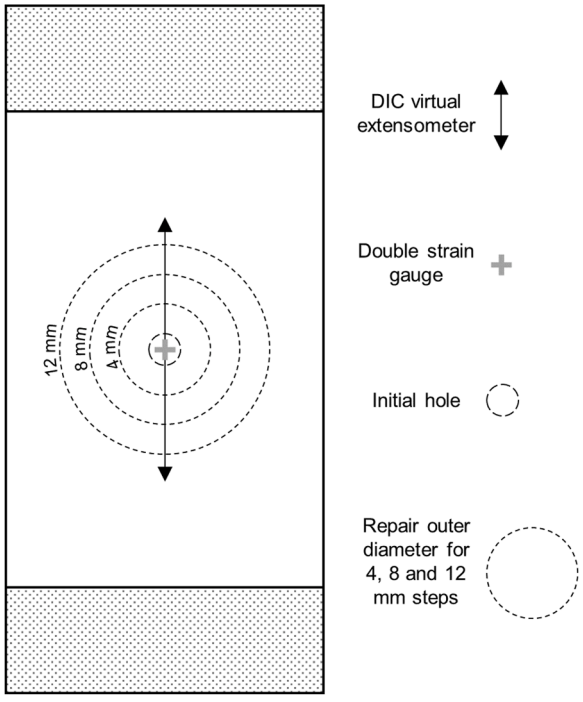

Fig. 6. Schematic representation of a repaired panel with the DIC extensometer and strain gauge.

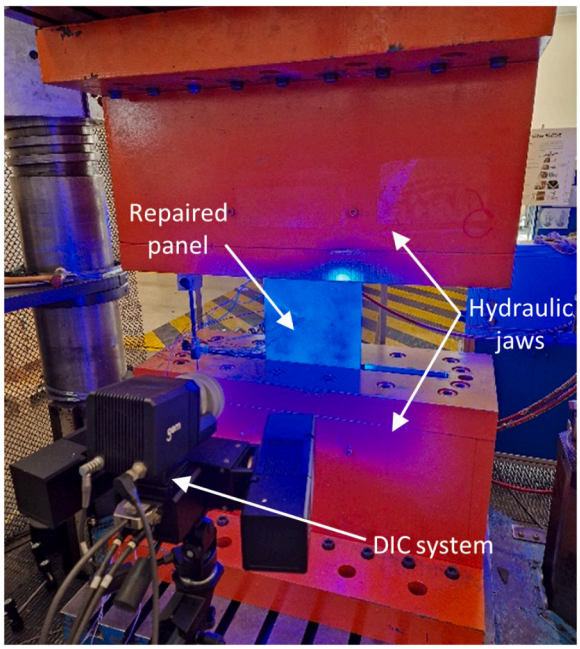

Fig. 7. Tension testing setup for repaired panels.

3.1. Geometry and mesh

The axis system used is given in Fig. 1. The X-axis is set in the direction of the load, the Y-axis in the width of the specimens, and the Z-axis through the thickness of the laminates. The 2D GPS model (Fig. 8) uses the geometry of repaired coupons reduced to one-half by taking advantage of their symmetry plane at the centre of the patch. The 3D Panel model uses the geometry of stepped repaired panels but modelling only a quarter of it thanks to its two symmetry planes along its length and width (Fig. 9). These symmetries are preserved even in presence of 45° plies because the G939 is a balanced woven fabric. The 2D GPS is not only meant to study the behaviour of the repaired coupons, but also to investigate to what extent it can be representative for the behaviour of repaired panels.

The meshing strategies of both models are similar. One layer of 8-nodes continuum shell elements with reduced integration (SC8R) was used for each ply of the parent structure and the repair patch, with a 0.24 mm thickness to match the nominal thickness of G939/M18 plies. Repair plies made of G939/Hexbond 312-L were modelled using the same thickness. A layer of 8-nodes cohesive elements (COH3D8) with a thickness of 10^{-4} mm was inserted between each ply of composite to be able to simulate the delamination inside the laminates by CZM. One layer of cohesive elements of thickness 0.1 mm was used to model the adhesive material at the interface between the repair patch and the parent plate, driving the behaviour of the stepped joint using also CZM (Fig. 8).

To mesh the specimens in 2D GPS, a single element of 1 mm width was used in the width direction of the model (Y-axis), instead of using the real width of the specimen to save computation time. In the 3D Panel model, 60 elements were used around the perimeter of the quarter repair. The 2D GPS and 3D Panel models were split in two areas: the zone of interest including the repair and a 5 mm area around it, and the rest of the model. An element length of 0.1 mm was used in the zone of interest, and a size of 5 mm was used outside of the zone of interest,

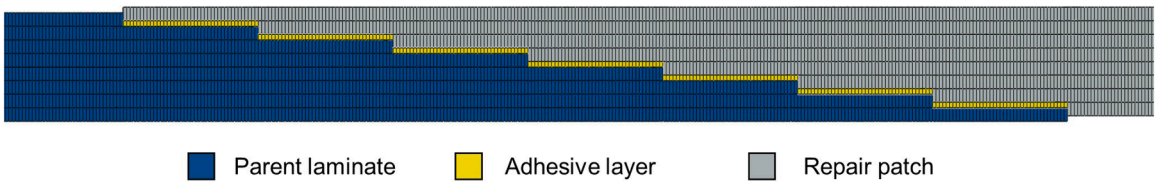

Fig. 8. Stepped joint meshing in the 2D GPS model.

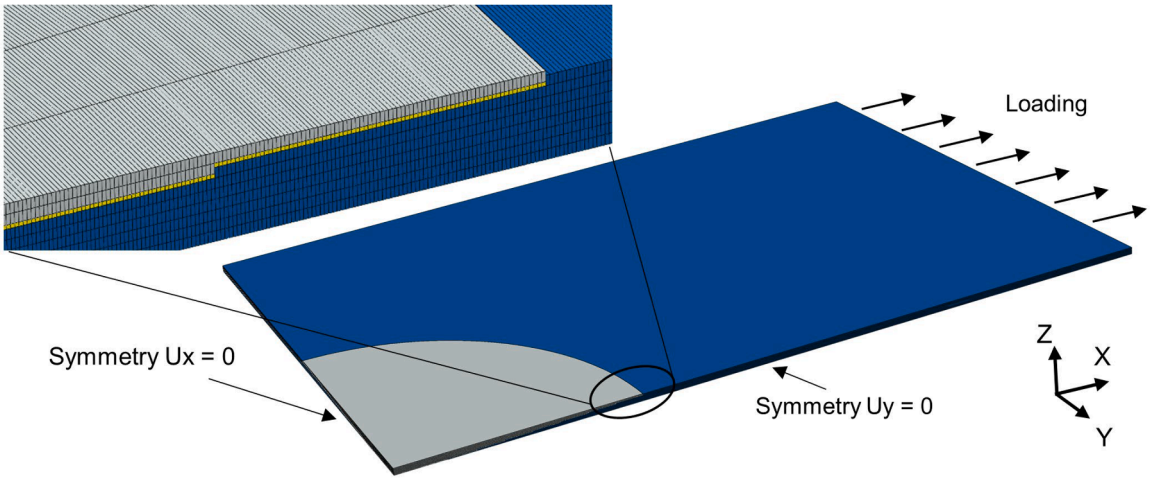

Fig. 9. 3D modelling of a stepped repaired panel.

again to save computation time. With those mesh parameters, nearly 200,000 elements were used in the 3D model of the quarter stepped repair panel with 12 mm steps, against 15,315 elements for the 2D GPS model with the same repair configuration.

3.2. Boundary conditions

A set of custom boundary conditions were used in the 2D GPS model to create a generalized plane strain state. A boundary condition $U_Y = 0$ was imposed one of the side faces of the model. On the other side face, an equation constraint was used to enforce the nodes of the face to have the same transverse displacement U_Y. Those two conditions together ensure that the strain in the direction Y of the model remains constant through the whole structure. A symmetry condition $U_X = 0$ was imposed on the plane of symmetry located on the patch side of the model, and the other side was clamped. The load was then applied by an imposed displacement of the parent side along direction X, until failure of the specimen.

In the 3D Panel model (Fig. 9), $U_X = 0$ and $U_Y = 0$ were respectively applied to the side faces of the model to enforce the symmetry conditions. The loading edge was clamped and an imposed displacement along the X direction was imposed until failure.

3.3. Damage modelling

3.3.1. Cohesive zone modelling

Cohesive zone modelling (CZM) is it an efficient way to model progressive failure of adhesive layers or delamination of composite laminates, as it allows to simulate the initiation and propagation of a crack along a predefined path. To do so, it uses traction-separation laws with a softening shape that accounts for the damage evolution. Various laws shape can be used to model bonded joints, such as triangle, trapezoidal and exponential laws. Previous studies showed that the choice of the law shape may have a little influence CFRP bonded repairs simulations, but without major discrepancies between the results obtained with each shape [10,31].

In this study, CZM was used in FE simulations with the Abaqus software to model the behaviour of the Hexbond 312-L adhesive interface between the parent plate and the repair patch, and to model delamination in G939/M18 and G939/Hexbond 312-L laminates. A triangle law shape (Fig. 10) was used for the adhesive interface and for delamination. Material parameters used are given Table 3. The law is defined in pure mode I and II by the interface stress, damage initiation stress and fracture energy. In each pure mode, before reaching the initiation stress, the cohesive law results in a linear elastic behaviour with a stiffness k_i. After the initiation stress is exceeded, the damage variable D increases and the stiffness decreases accordingly. To handle mixed-mode behaviour, quadratic stress initiation criterion was used:

$$\left(\frac{\langle\sigma_n\rangle}{\sigma_{\mathrm{I}}^0}\right)^2 + \left(\frac{\langle\sigma_s\rangle}{\sigma_{\mathrm{II}}^0}\right)^2 = 1 \tag{1}$$

Where σ_n (σ_s) are the normal (shear) interface stress, and σ_{I}^0(σ_{II}^0) are the mode I (mode II) maximum interface stress. Benzeggagh-Kenane damage evolution criterion with an exponent $\eta = 1$ was used to determine mixed mode fracture energy:

$$G_{\mathrm{C}} = G_{\mathrm{IC}} + (G_{\mathrm{IIC}} - G_{\mathrm{IC}})\left(\frac{G_{\mathrm{II}}}{G_{\mathrm{I}} + G_{\mathrm{II}}}\right)^{\eta} \tag{2}$$

Where G_i is the strain energy release rate in mode i ($i = I,\ II$) and with and G_{C} is the mixed-mode fracture energy. Mathematical details about the implementation of triangle law in Abaqus and the damage variable computation can be found in the Abaqus analysis user guide [40]

3.3.2. Continuum damage mechanics for CFRP

Continuum damage mechanics (CDM) were used to model the intralaminar failure behaviour of the parent plate and the repair patch. Unlike CZM, CDM allows to compute the initiation and propagation of damage inside a material without predefining a crack path, at the price of being computationally intensive. To do so, plane-stress Hashin's failure criterion was used for damage initiation inside the laminates,

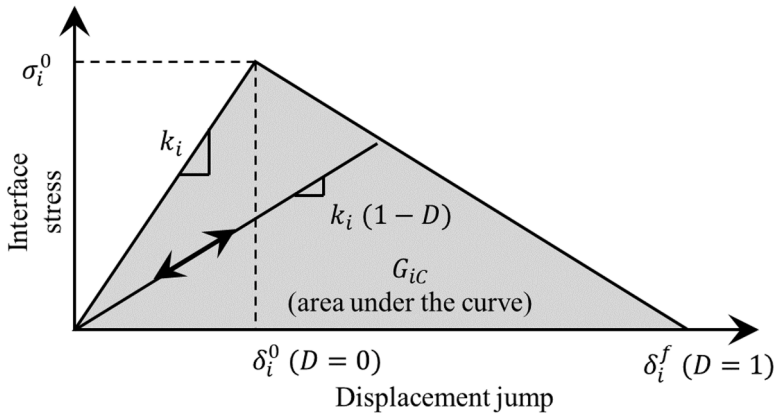

Fig. 10. Bi-linear traction separation law [31].

coupled with linear damage evolution based on intralamianar fracture energy. This damage evolution is driven by the same types of triangle laws that are used for cohesive laws (Fig. 10). In the case of woven fabric laminates, the usual writing of Hashin's criterion in terms of fibre and matrix criterion makes less sense because there are fibres in the longitudinal and transversal direction of the laminates. Thus, matrix properties were set equal to fibre properties in Abaqus and a tension/shear coupling coefficient $\alpha = 1$ was used, so that fibre tension initiation criterion in longitudinal and transversal directions are identical. For an illustration purpose, the Hashin's initiation criterions for tension loading with those parameters are written as follows:

$$\left(\frac{\widehat{\sigma}_{11}}{X_T}\right)^2 + \left(\frac{\widehat{\tau}_{12}}{S_{12}}\right)^2 = 1 \tag{3}$$

$$\left(\frac{\widehat{\sigma}_{22}}{Y_T}\right)^2 + \left(\frac{\widehat{\tau}_{12}}{S_{12}}\right)^2 = 1 \tag{4}$$

Where $\widehat{\sigma}_{11}$, $\widehat{\sigma}_{22}$, $\widehat{\tau}_{12}$ are the components of the effective stress tensor $\widehat{\sigma}$ that is computed from $\widehat{\sigma} = M\sigma$ where M is the damage operator, which depends on the damage variables and σ the true stress. The other notations are detailed in Table 2. The damage variables for each damage mode are computed using:

$$d = \frac{\delta_{eq}^f\left(\delta_{eq} - \delta_{eq}^0\right)}{\delta_{eq}\left(\delta_{eq}^f - \delta_{eq}^0\right)} \tag{5}$$

Where δ_{eq}^0 $\left(\delta_{eq}^f\right)$ are the equivalent displacements at damage initiation (propagation), as defined in Fig. 10. The current equivalent displacement δ_{eq} is computed from the stress and strains associated to each damage mode. For instance in fibre tension:

$$\delta_{eq}^{ft} = L^c\sqrt{\langle\epsilon_{11}\rangle^2 + \epsilon_{12}{}^2} \tag{6}$$

Where L^c is a characteristic length determined by Abaqus based on the element geometry and formulation. In the case of a first order element is the typical length of a line across the element. Mathematical precisions about the initiation criterion and computation of damage variable and damage evolution can be found in the Abaqus user analysis guide [41].

Table 2
CFRP intralaminar properties used for FE modelling.

Property	Symbol (unit)	Value	
		G939/M18	G939/Hexbond 312-L
Young modulus	$E_{11} = E_{22}$ (MPa)	59000	59000
Poisson ratio	ν_{12}	0.05	0.05
In-plane shear modulus	G_{12} (MPa)	4200	3050
Out-of-plane shear modulus	$G_{13} = G_{23}$ (MPa)	4050	3000
Tensile failure stress	$X_T = Y_T$ (MPa)	850	840
Compressive failure stress	$X_C = Y_C$ (MPa)	800	800
In-plane shear failure stress	S_{12} (MPa)	107	82
Out-of-plane shear failure stress	S_{23} (MPa)	107	82
Fibre tensile fracture energy	$G_{C,ft}$ (kJ/m^2)	25	25
Fibre compressive fracture energy	$G_{C,fc}$ (kJ/m^2)	25	25

3.4. Material properties

There is existing data on the in-plane properties of G939/M18 [42], however there is no data available on G939/Hexbond 312-L and only very little data on Hexbond 312-L [43–45]. Thus, a large test campaign was carried out to identify the material properties that are needed for finite element (FE) modelling. This test campaign is not extensively detailed in this paper and a brief description of the tests that were carried out is provided instead.

Properties used to model the intralaminar behaviour of G939/M18 and G939/Hexbond 312-L are summarized in Table 2, where subscripts 1, 2 and 3, refers respectively to warp, weft, and through-the-thickness direction of the fabric, and X and Y respectively refers to strength in warp and weft directions. As FE modelling was done using shell elements for the laminates, the out-of-plane modulus E_{33} was not required. To reduce the number of tests, it was supposed that the composite materials had an orthotropic behaviour with $E_{11} = E_{22}$, $G_{13} = G_{23}$ and $X_T = Y_T$ and $X_C = Y_C$, since G939 is a balanced woven fabric. Tensions tests on 16-plies-thick specimens oriented at 0° were carried out to identify E_{11}, ν_{12} and X_T. Compression tests at 0° were carried out to identify X_C. Tensions tests at 45° were performed to identify G_{12} and S_{12}. S_{23} was set equal to S_{12} as there is no significant out of plane shear effect in this problem. Out-of-plane shear modulus G_{13} was measured by 3 points bending tests on large specimens with a thickness of 10 mm, monitored by DIC. Fibre tensile fracture energy $G_{C,ft}$ of G939 fabric was measured by compact tension tests on G939/M18 specimens. Because the problem studied is a stepped repair loaded in tension, compression properties of the laminates do not have significant influence on the results. Thus, fibre compressive fracture energy $G_{C,fc}$ was set equal to fibre tensile fracture energy $G_{C,ft}$.

Properties used for CZM of delamination inside the adherends, and disbonding of the adhesive interface are summarized in Table 3. G939/M18 and G939/Hexbond 312-L delamination fracture energy in Mode I and II G_{IC} and G_{IIC} were measured by DCB and 4ENF tests. 20 plies-thick-specimens were used, with a PTFE film of thickness 0.007mm inserted in the middle to create an initial crack. Delamination interface stiffness and

Table 3
Delamination and adhesive properties used for CZM.

Property	Symbol (unit)	Value		
		Hexbond 312-L parent/patch	G939/M18 delamination	G939/Hexbond-312L delamination
Mode I interface stiffness	k_I (N/mm^3)	24000	1.10^6	1.10^6
Mode II interface stiffness	k_{II} (N/mm^3)	8000	1.10^6	1.10^6
Mode I initiation stress	σ_I^0 (MPa)	68	50	50
Mode II initiation stress	σ_{II}^0 (MPa)	48	50	50
Mode I fracture energy	G_{IC} (kJ/m^2)	2	0.4	1.3
Mode II fracture energy	G_{IIC} (kJ/m^2)	4.5	1	2.5

peak stresses were not experimentally measured, as G_{IC} and G_{IIC} drive the delamination behaviour. Instead, those parameters were set at typical values used to model delamination of an epoxy matrix by cohesive zone modelling, namely 1.10^6 N/mm^3 for the interface stiffness based on the guidelines of Turon et al., and peak stresses of 50 MPa [46].

Hexbond 312-L behaviour was studied at confined state, as it is in a repair, using aluminium adherends and a surface treatment that allows cohesive failure of the bonded joints to be obtained. DCB and 4ENF tests were performed to identify the adhesive fracture toughness in mode I and II. Butt Joint and Thick Adherend Shear Tests (TAST) were carried out to measure the tensile and shear maximum stress of the adhesive, and to identify its elastic modulii $E = 2400$ *MPa* and $G = 800$ *MPa*. The Hexbond 312-L interface stiffnesses in the repair was determined using $k_I = E/t_a$ and $k_{II} = G/t_a$ where $t_a = 0.1$ mm is the adhesive film nominal thickness.

3.5. Mesh study

A mesh study was performed on the 2D GPS model to make sure that the element length chosen is small enough to compute failure of the composite adherends. Simulations with mesh size of 1, 0.5, 0.2, 0.1 and 0.05 mm were compared in terms of failure strength of a repaired coupon with a step length of 8 mm (Fig. 11). The element length does not influence on failure load when it is smaller than 0.1 mm. Because the stress state along the bondline in the 3D Panel model is similar to the one of the 2D GPS model [31], the mesh study on the 2D GPS model ensures that the chosen mesh size is appropriate for the 3D Panel model.

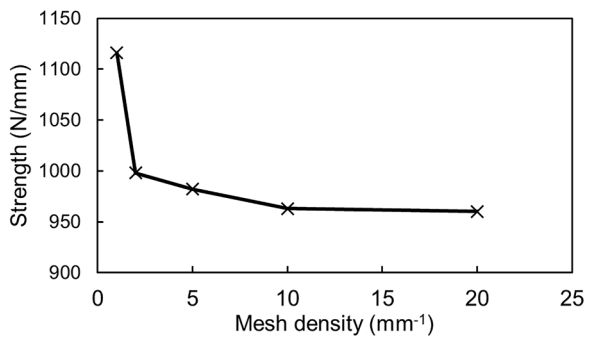

Fig. 11. FE 2D GPS meh convergence study with CFRP damage modelling.

4. Results and discussions

4.1. Fracture patterns

4.1.1. Experimental observations

Failure of the coupons under tension loading always occurred in the area where the parent plate and the repair patch overlap each other. Coupons broke into 2, 3 or 4 pieces, meaning there can be several fracture locations on the same specimen. Among the tested coupons: two main types of fracture patterns were encountered. The first one, named type A (Fig. 12), is neat failure of the composite laminates with no visible sign of disbonding of the patch, featuring fibre fracture and some interlaminar cracks of variable length near the fractured area. The location of this neat fracture is variable from one specimen to another (see section 4.1.3). The second fracture pattern, named type B (Fig. 12), is a mixed failure featuring fibre fracture of the composite laminates and disbonding of the repair over a part of the bonded joint. The latter happens about the middle of the stepped joint, and appears to be mix of adhesive failure, cohesive failure and matrix cracking. Among the coupons, type B failure occurred only in the C-T-4M configuration, namely through repaired coupons with 4 mm steps, while type A failure was the only one observed among the other repaired coupon configurations.

The same types of fracture patterns were observed on the repaired panel specimens (Fig. 13). Type A only was encountered for steps length of 8 and 12 mm. The crack path on repaired-panels goes from one edge to the other and passing through the patch area. It is clearly visible that the crack path follows the end of one of the repairs steps, in a circular shape, right at the centre of panels. It confirms that step ends are the weak spots of the repaired panels. Type B failure was encountered on panels with 4 mm steps, in two specimens out of three. In that case, there is a crack going from side to side in the parent plate, but a part of the repair patch was visibly disbonded from the parent plate. Therefore, it can be concluded that the failure mechanism encountered in repaired coupons are consistent with the one of repaired panels. A summary of the failure types and locations is provided in Table 4 and is discussed in section 4.1.3 in comparison to FE results.

4.1.2. Numerical progressive damage analysis

In 2D GPS FE simulations, type A fracture pattern was obtained, involving fibre fracture and interlaminar cracking near the failure spot (Fig. 14) as it was observed experimentally. During the loading, all the step ends become areas of stress concentration inside the laminates. The analysis of Hashin's criterion for fibre fracture in tension (HSNFTCRT) allows highlighting those stress concentrations. In this study, HSNFTCRT is used as the initiation criterion, and is coupled to a damage evolution law. It would be overly conservative to use it alone as the final failure indicator, as it reaches the value 1 at 70 % of the maximum load completed with damage evolution. The fibre tension damage variable (Fig. 15) is the actual failure indicator. The presence of stress concentration at multiple steps ends is compatible with the variety of failure locations spotted experimentally as described in the next section. Failure eventually happens in the 0° ply located under the first repair step, right under the beginning of the first step. The rest of the plies then progressively fracture one after another through the whole laminate thickness, resulting in the same neat failure that was observed experimentally.

When it comes to local effects (Fig. 15), the Hashin's matrix tension criterion is similar to the fibre tension criterion in 45/-45° plies. This was expected given how the woven composite material was modelled in the analysis. The top 45° ply reaches its maximum load carrying capacity at 83 % of the maximum load at step end number 1. The end part of this 45° ply going between step #1 and step #0 is visibly unloaded, redistributing the load to the rest of the structure. This effect is quite interesting, given that peeling effects at stepped and scarf repairs end are often mentioned to be significant [11]. Yet, in the present case, the end plies at the top of the repairs does not carry much load as in can be seen

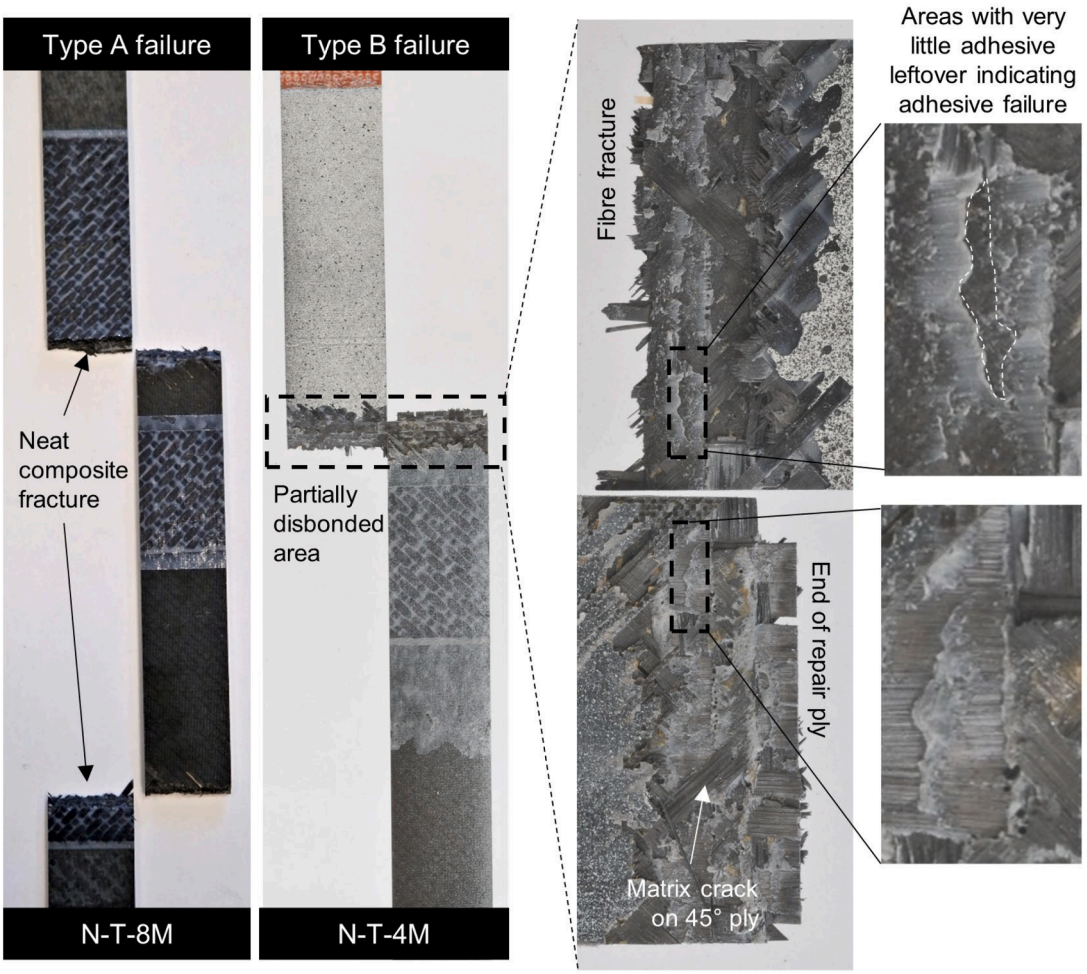

Fig. 12. Macroscopic view of the fracture morphology of stepped repaired coupons.

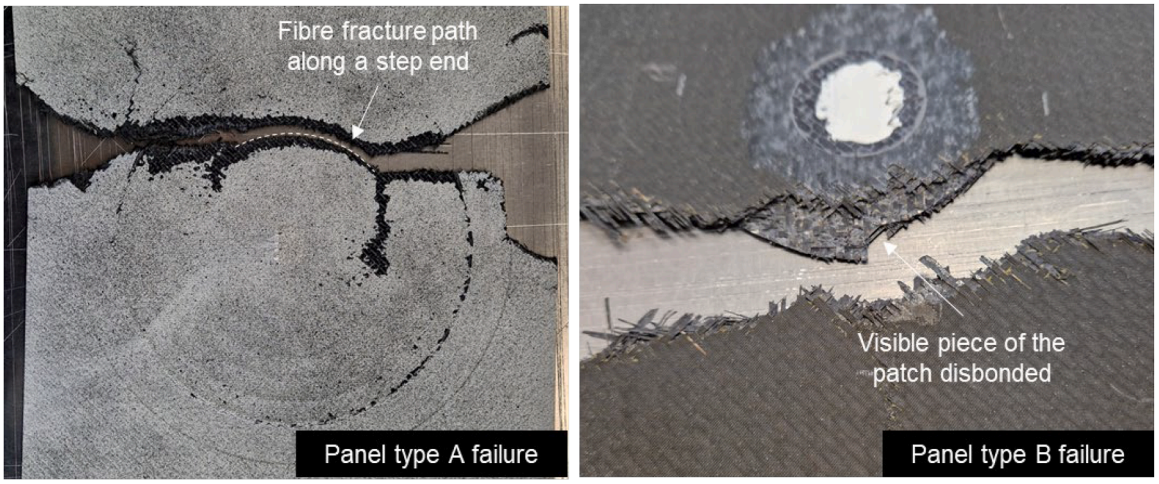

Fig. 13. Macroscopic view of the fracture morphology of stepped repaired panels.

through the present analysis. (Section 3.3.2). The fibre tension damage variable progresses only at the step end #0 and in the top 45° ply at step #1 as explained. Fibre damage does not evolve at the other step ends even though the fibre tension initiation criterion is met. Delamination effects are visible inside the parent laminate at step end #0 where failure occurs. However, the adhesive layer between the patch and the parent plate does not fail and the patch remains bonded to the parent plate after failure, as shown by the scalar stiffness degradation of cohesive zones, also called SDEG variable in Abaqus. The two latter observations are representative for the experimental fracture patterns observed in case of failure type A, featuring neat laminate failure with local delamination but no patch disbonding.

In the 3D panel model, type A fracture with a crack going along one of the step ends was obtained (Fig. 16), in agreement with experimental

Table 4
Failure types and locations.

Specimen set	Failure location (* indicates it was encountered more than half of the time)	Failure type	FE 2D GPS failure scenario	FE 3D Panel failure scenario
C-NT-4M	0* / 6	A	0A	-
C-NT-8M	3* / 1 / 2	A	3A	-
C-NT-12M	3* / 0	A	3A	-
C-T-4M	1 / 3 / 4	B	0A	-
C-T-8M	0 / 1 / 3	A	0A	-
C-T-12M	3* / 0 / 1	A	0A	-
P-T-4M	2 / 3 / 4	A / B	-	3A
P-T-8M	3* / 4	A	-	3A
P-T-12M	3*	A	-	3A
C-NT-8O	3* / 0	A	3A	-
C-T-8O	0 / 3 / 5	A	3A	-
C-T-8M*	-1 / 0 / 3 / 4	A	0A	-

observations. Like in 2D GPS simulations, the fibre failure initiation criterion is met at several locations, and especially at step ends #1 #3 and #4. The local effects associated with the composite laminates failure in the 3D model are similar to the ones identified in the 2D model. In particular, the upper 45° ply at the step end #1 that reaches his maximum load carrying capacity before the final failure, unloading the end of this ply and redistributing the load to the rest of the steps. Fig. 17 highlights the evolution of the fibre tension criterion in the parent structure and the repair patch separately.

It appears that the middle section of the repaired panels is indeed the most loaded section, even though the surface 45° plie does not reach a value of 1 of the fibre tension criterion (Fig. 16). Stress concentrations are located at the steps ends around a 45° arc on both sides of the most loaded section. In the studied configuration, FE simulation predict a simultaneous failure of the repair patch and the parent material, as there is no clear sign of early failure in one of the these.

Failure type B was not predicted by FE models for C-T-4M specimens as it was observed in experiments (Fig. 16). Instead, a failure type A with fibre fracture was obtained. Two hypotheses can be formulated to explain this discrepancy. On the one hand, repaired coupons with 4 mm steps are particularly vulnerable to defects in the repair process. With such short steps, a small misalignment of the patch results in a high relative loss of step length, resulting in an early disbonding of the patch. On the other hand, it could come from a coupling effect between the composite laminate fracture and the disbonding of the patch, i.e. the damage mechanism at the interface between the patch and the parent plates and inside the laminates acting together, that is not present in the FE model. Decreasing step lengths were tested in 2D GPS models until obtaining a disbonding of the patch with a 3.5 mm step length (Fig. 18). A more comprehensive analysis of cohesive failure of stepped joints simulated by FE is available in [30] and [31].

The failure scenario obtained does not feature both disbonding and fibre fracture as it is in failure type B. It consists in a complete disbonding of the patch. These results show that the C-T-4M configuration is theoretically close to the disbonding failure mode. It is compatible with the two hypotheses made on failure type B, namely high sensitivity to step length defect, and the lack of coupling mechanism between disbonding and laminate failure in the FE models.

4.1.3. *Comparison between experimental and numerical failure location*

Measurements of the failure locations were performed with to identify precisely where it occurs. On repaired panels, this measurement was done on the centreline of the specimen. It was concluded that type A failure always happened at the end of one of the repairs steps of the coupons and panels, confirming that steps ends are the weak spots of the laminates due to stress concentrations as highlighted by the FE simulations.

Fig. 19 brings a comparison between the experimental failure path of a P-T-8M specimen and the FE results of the associated model. It can be clearly seen that the failure path of the specimen follows the circular shape of a step end. The FE model can predict accurately this failure path. It shows that that this type of numerical modelling can identify the weak spot of a stepped repaired panel.

When it comes to repaired coupons, the failure locations reported by the tension tests are not as deterministic as the FE simulations. Fig. 20 highlights the failure locations of the C-T-8M* specimens as an example. Several different fracture locations were often reported within the same set of specimens, and sometimes two different locations were reported on the same specimen. This is generally the case for other configurations tested. The FE results predict one the failure locations that was experimentally obtained at step #3, unlike the C-T-8M which was predicted to fail at step #0 on the parent side (Fig. 14). This location was encountered on 3 specimens out of 5 tested. It can also be seen that failure may happens outside of the repaired area.

To give an overview of all the different failure behaviour encounter among the tested specimens, all failure types and locations that were encountered are summarized in Table 4 and compared to FE results, based on the steps numbering provided in Fig. 2. There is a good agreement between simulation results and experimental observations.

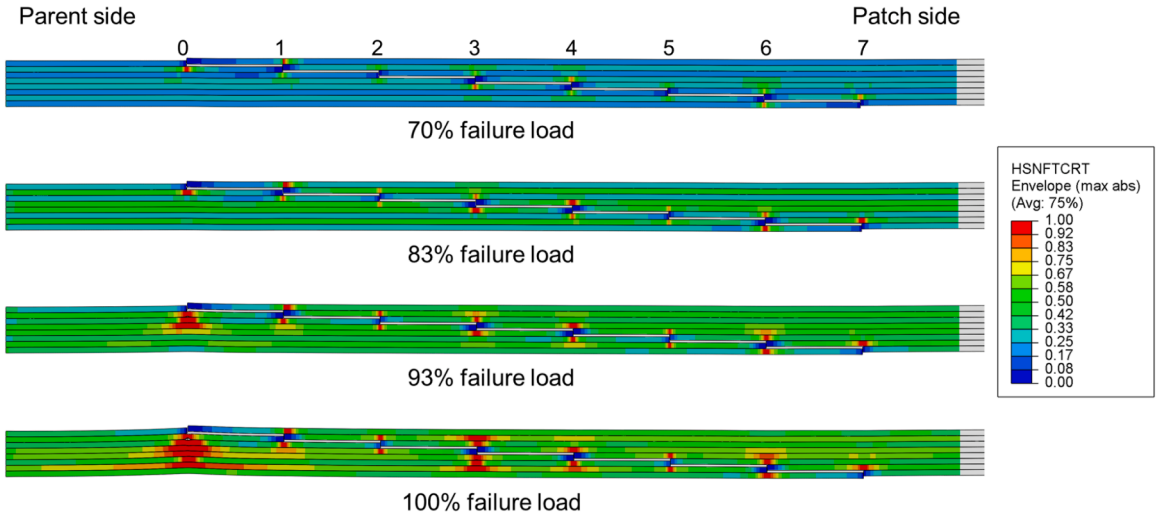

Fig. 14. FE progressive damage analysis by 2D GPS modelling of the C-T-8M configuration. Specimen thickness was magnified 2x for better readability. HSNFTCRT is Hashin's fibre tension criterion. Steps number from 0 to 7 are reminided.

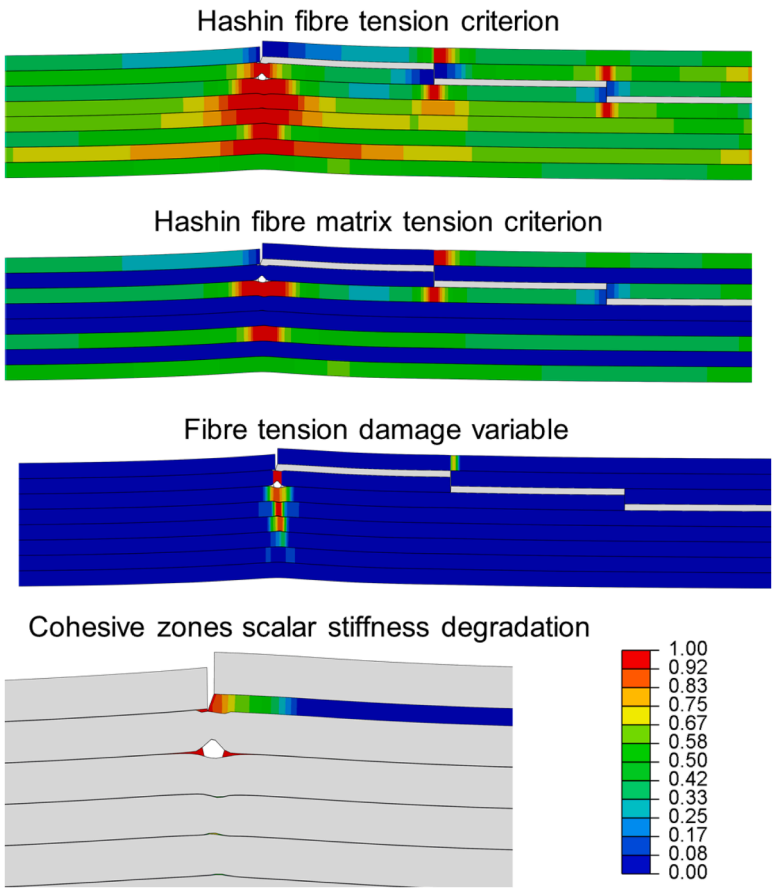

Fig. 15. Local analysis of the failure mechanisms in the C-T-8M configuration at 100 % of failure load. The 0 to 1 color scale applies to all the displayed criterion and variables.

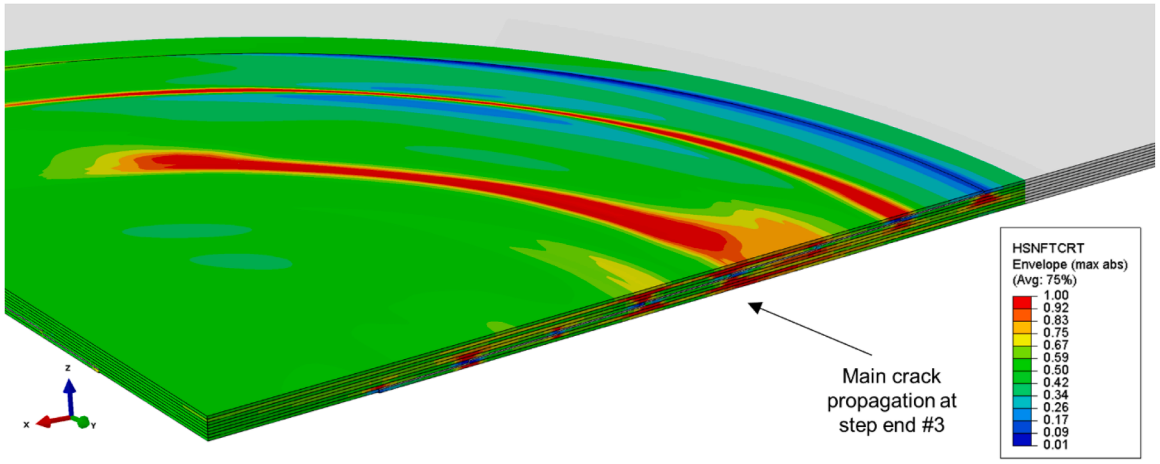

Fig. 16. FE 3D panel failure scenario in P-T-8-M configuration. HSNFTCRT is the Hashin's fibre tension criterion.

When it comes to the experimental failure type A, FE models always predict a failure location that happened experimentally, and often the most encountered one. Type A failure locations predicted 2D GPS and 3D Panel model with the same repair configuration are nonetheless different: it occurs at step end #0 in the first model and at step end #3 in the second model. However, step end #3 is the second most damaged spot in the FE 2D GPS model (Fig. 14). Thus, even though 3D effects in the full-scale model may shift the failure spot to a different location, the stress state of the laminates in the 2D GPS models remains close to the most loaded section of the 3D model. Type B failure happened mainly between step ends number #3 and #5, which is compatible with the failure scenario of the 2D GPS model with a 3.5 mm step length.

To pursue the investigation of the deviations between the FE failure scenario and experimental results on C-T-4M specimens, microscopic observations were performed on the leftover material that remained after cutting these coupons. Two samples were embedded in resin and then carefully polished to be able to observe (XZ) sections of the repair, as presented in Fig. 2. This allows understanding how repair plies are positioned in relation to repairs steps ends. Thanks to these microscopic observations, some repair ply positioning defects were found. An

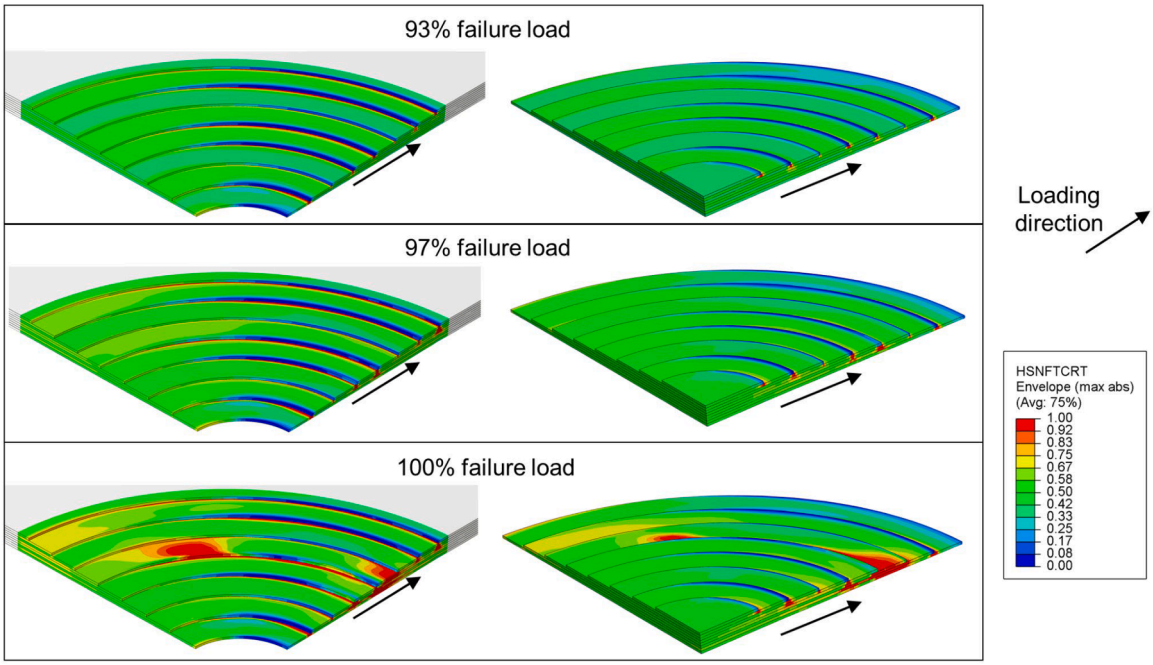

Fig. 17. Evolution of Hashin's fibre tension criterion (HSNFTCRT) in the parent structure and the repair patch when approaching the ultimate load in the P-T-8M configuration.

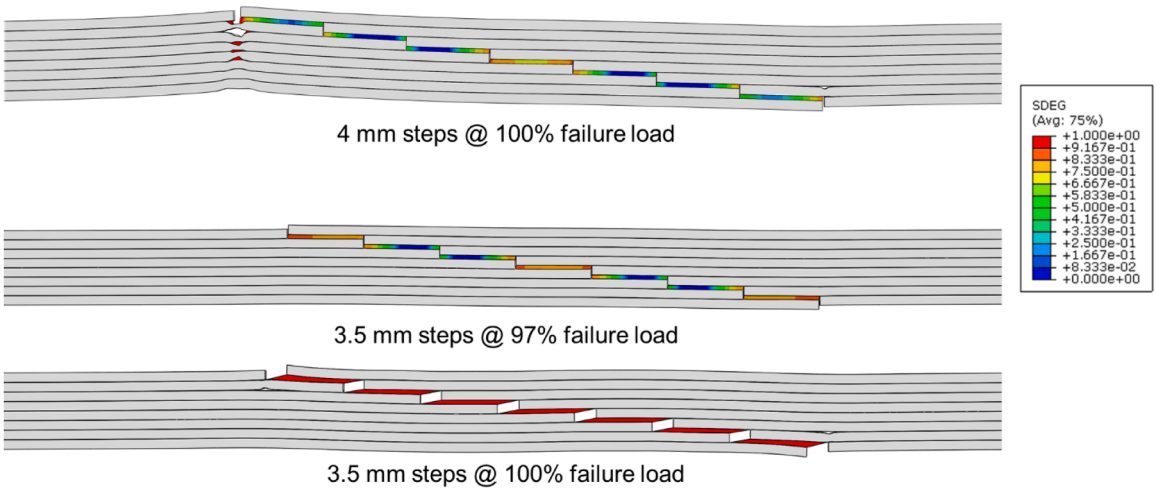

Fig. 18. FE 2D GPS failure scenario in C-T-4M configuration. SDEG is the damage variable of the cohesive elements modelling the adhesive material.

example of positioning defect of a repair ply is provided in Fig. 21. Gaps going from 0.2 mm to 0.75 mm were measured between the corner of a step and the associated repair ply, and there was a good agreement between the observations of the same step end on the two samples. These experimental observations are compatible with the results of the FE simulations with a step length reduced to 3.5 mm (Fig. 17).

To conclude this section, these results extend the conclusions of [30] and [31], by showing that 2D and 3D FE models with damage modelling of the composite adherends (i) have similar failure scenarios and (ii) agree with experimental observations.

4.2. Repair strength

4.2.1. Overall mechanical response

Elongation of the panels was computed by DIC measurements (Section 2.4), to bring a measurement of the response of the structure under the tension loading. DIC data was preferred to the displacement measurement provided by the 3000 kN testing machine because the latter tends to include to machine stiffness to the results, and therefore make the specimens stiffness appearing lower that it actually is. As a matter of example, the elongation-load curves of the P-T-8M specimens, C-T-8M specimens and the FE simulation results are presented in Fig. 22. The experimental data shows a linear behaviour of the coupons and the panels, followed by an instantaneous failure. The FE results are in good agreement with the experimental data, with a slightly stiffer response. The same type of linear behaviour followed by an instantaneous failure for panels with 4 mm, 8 mm and 12 mm steps, and for repaired coupons.

4.2.2. Effect of patch stacking sequence

The experimental and numerical results obtained for the three sets of through repaired coupons with a step length of 8 mm and different patch layups are presented in Fig. 23. Because these specimens are through repaired coupons, the entire load has to be transferred by the bonded joint when the specimen is loaded in tension. The C-T-8M configuration

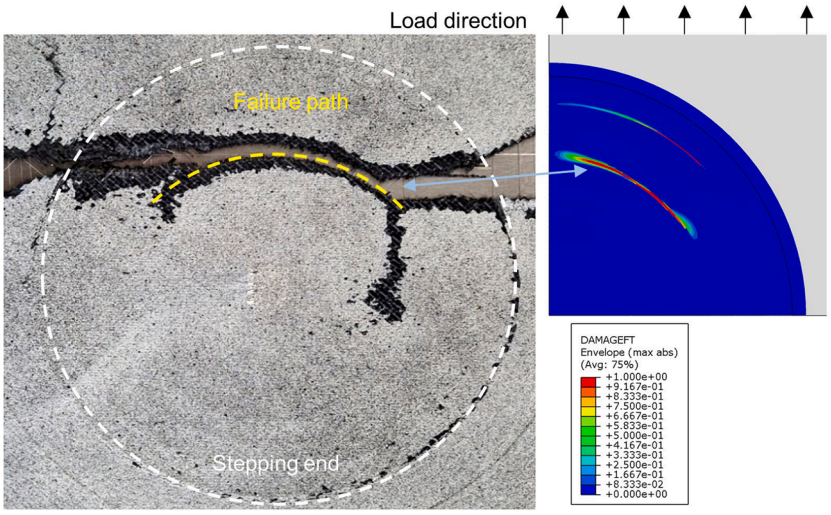

Fig. 19. Comparison of experimental failure path and FE failure path computed thank to progressive damage analysis. DAMAGMT is the damage variable associated with fibre failure of the composite material.

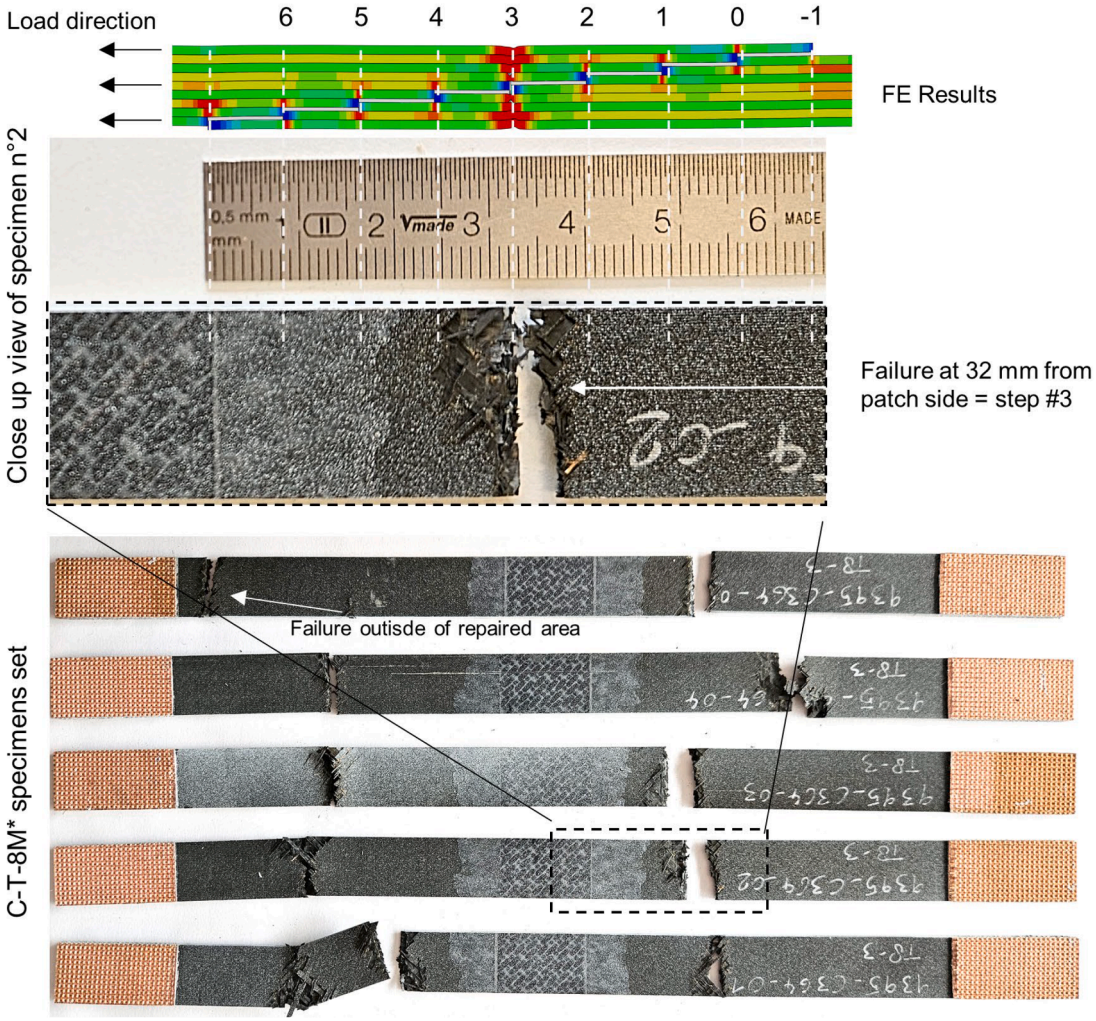

Fig. 20. C-T-M8* specimens failure location and FEM results associated.

has the lower strength, follow by the C-T-8O configuration and then the C-T-8M* configuration with the highest strength. When comparing those results to the tensile strength measured for the parent material alone, it appears that there is no significant deviation between the C-T-8M* strength and the parent plate strength, given the dispersion of the results. The associated strength recovery rate is about 100%. There is an

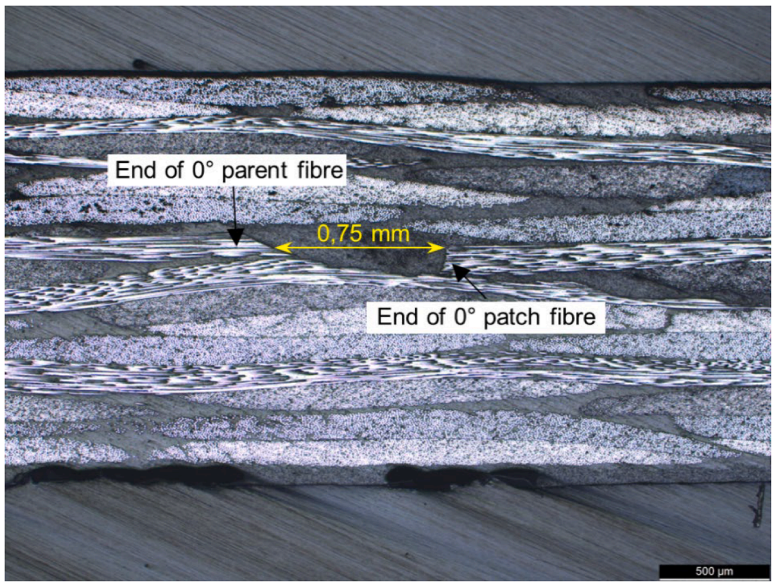

Fig. 21. Microscopic view at 50x magnification of a section of a stepped repaired coupon.

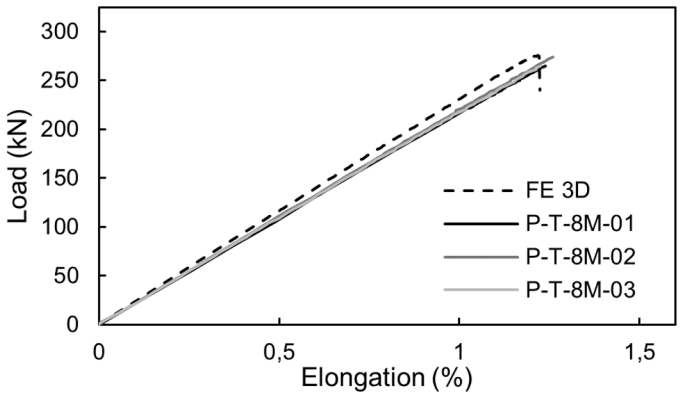

Fig. 22. Load - elongation curves of P-T-8M specimens. Elongation refers to the longitudinal strain of the specimens measured by the DIC extensometer.

excellent agreement between experimental results and numerical results for C-T-8M specimens and C-T-8O specimens, with less than 2 % deviation, and a good agreement for C-T-8M* specimens with less than 5 % deviation. The numerical FE 2D GPS tends to overestimate the strength of the first two configurations and underestimate the strength of the last one. Nonetheless, it predicts that the C-T-8M*configuration do indeed have higher strength than the C-T-8O configuration, as shown by experimental results. In terms of stiffness, the addition of overplies contribute to make the coupons stiffer, as it can be expected. The FE simulation agree with the experimental results on that tendency, while being slightly stiffer, about 5%, than the latter.

The results of the C-T-8M* tests show that it is possible to achieve a through-repair on a coupon that can restore the initial strength of the pristine laminate. It means that the bonded joint is strong enough not to be the weak link of the repair, and that the repaired laminate is able to withstand the stress concentration at the end of the steps. These results consolidate the conclusions that the bonded joint is not always the weak link in a stepped repair [39,47]. However, this conclusion remains limited to strength recovery rate of the repair under static loading: the repair is not likely to recover fully the initial durability of the pristine laminate, when subjected to hot-wet aging for example. When it comes to the repair patch layup, the results of this study dispute the common idea that an overlapping layup (O) of the patch, where each repair ply is bonded to a parent ply of same orientation, is needed to achieve a proper repair. This could be explained by the fact that proposed matching patch layup plus 0° overply (M*) allows using one more 0° ply than the standard overlapping patch configuration with the same total number of plies.

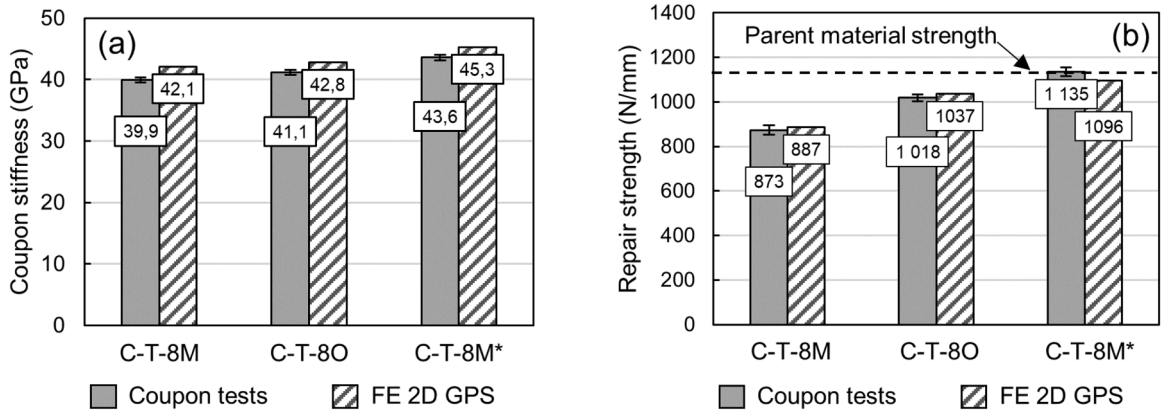

Fig. 23. Effect of patch layup on repair stiffness (a) and strength (b).

4.2.3. Effect of step length, damage depth and specimen scale

The measured stiffness (Fig. 24) and repair strength (Fig. 25) of the C-NT-xM, C-T-xM and P-T-xM (x = 4, 8, 12) specimens was analyzed compared to FE results. Repair strength is compared in terms of force flow (N/mm) to be able to compare coupons and panels of different widths. The effect of three variables can be studied thanks to this data, being step length, damage depth and specimen scale (coupon / panels). Overall, there is only little deviation between the experimental results of the nine configurations tested and FE results are in excellent agreement with experimental data. In terms of stiffness, FE models are a little stiffer than experimental tests. FE models are likely to be stiffer that tests because of (i) perfect boundary conditions hypothesis in the FE mode, while real BC may be less stiff, and (ii) perfect specimen alignment hypothesis in the FE model, while real testing setup might not be perfect because of a small misalignment between the ends of the machine. In terms of strength, there is also an excellent agreement between tests and simulations. C-T-4 M specimens are the only exception, as they have a lower strength than the others do. This particular point is discussed at the end of the section.

The following conclusions on the three parameters studied can be drawn from the experimental data. First, there is no strength increase of repaired panels and non-through repaired coupons beyond a step length of 4 mm steps, but through-repaired coupons do have an increase of strength when going from 4 mm steps to 8 mm. There also no significant effect of damage depth on the strength of repaired coupon with step length of 8 mm and 12 mm. It shows that deeper repairs may not be weaker than shallower ones if the step length is long enough. Finally, there is a good agreement between the strength of repaired panels (P-T-xM) and the equivalent coupons (C-T-xM) for step lengths of 8 mm and 12 mm, but C-T-4M specimens have a lower strength than their equivalent panels P-T-4M. Those three points are related to the same physical phenomenon, being the level of stress concentrations at the end of the repair step. Indeed, when the step length is long enough to ensure that the bonded joint is not the weak link of the repair, the stress concentrations inside the laminates drive the behaviour of the repairs as highlighted by FE simulation (section 4.1.2). These levels of stress are directly related to the stress state along the bondline of the repair. Furthermore, it was shown by a previous study [31] on stepped joints that the levels of stress along the bondline barely depends on the step length within a range from 3 to 12 mm and are similar in the most loaded section of a repaired panel and its equivalent stepped joints.

The present experimental results confirm that there is step length threshold, beyond which no increase of the repair static is obtained. Regarding the “equivalent joint” question, it can be concluded that that tests at the scale of coupon allow measuring, conservatively, the strength of the associated stepped repaired panel. In addition, the 2D GPS modelling of stepped repairs is suitable to study the behaviour of a stepped repaired panel, including the strength and the failure mechanisms, hence providing a less-computation intensive modelling framework than full 3D models.

Yet, the lower strength of C-T-4M specimens compared to the C-NT-4M and P-T-4M ones indicates the field of validity of that last conclusion is to be discussed. This, behaviour of C-T-4M specimens can be related to C-T-4M specimens being close to patch disbonding as shown by FE results (section 4.1.2) and being the only ones with no alternative load path available than the bonded joint, which makes them more sensitive to manufacturing defects, as highlighted in section 4.1.3 (Fig. 21), and to possible coupling effects between disbonding of the joint and composite fracture. It could be reasonable to say that there is a zone around the step length where the transition between failure by disbonding of the joint and composite fracture occurs, inside which the behaviour of a coupon and a repaired panel may be more different. Moreover, repaired coupons are subjected to free-edges effect that do not exist in the centre section of a repaired panel, and it was shown be FE analysis in a previous study [31] that those effects tend to make the bondline of coupons weaker than the bondline of repaired panels, and weaker than predicted by a 2D GPS model.

4.3. Stress redistribution effect in repaired panels

Compared to coupons, stepped-repaired panels do have alternative load paths than portion of the bonded joint aligned with the direction of the load. For example, the load can be transferred by around the most loaded section of the bonded joint by the other parts of the bonded joints, or by the parent laminate. In both cases, this effect should results in a decrease of the load going through the centre of repaired patch compared to the average load applied to the specimen. The idea of the section is to discuss this “load bypass” effect, thanks to the strain gauges that were applied at the centre of the repaired panels. The mean longitudinal strain at the centre of the patch was computed as $\epsilon_p = (\epsilon_1 + \epsilon_2)/2$, where ϵ_1 and ϵ_2 are the strains measured by the gauges at the centre of the patch. It was then compared to the results FE simulations. The results of panels with 4 mm steps are presented in Fig. 26. The strain varies almost linearly with the applied load and there is a good agreement between the experimental data and the FE 3D Panel simulation. Nonetheless, there is a slight effect visible when the load approaches the ultimate stress of the repair. The strain measured by the central gauge increases more slowly than initially, indicating that the force flow through the patch begins to increase more slowly.

The stress inside the patch may not be measured directly, but the repair patch is the only material present at the centre hole of the panel. Hence it is possible to evaluate the force flow P_{patch} going through the centre of the patch as $P_{\text{patch}} = E_p \epsilon_p t_p$, where E_p is its Young modulus computed thanks classical laminate theory, t_p its thickness, ϵ_p the longitudinal strain measured. Knowing the mean force flow applied the

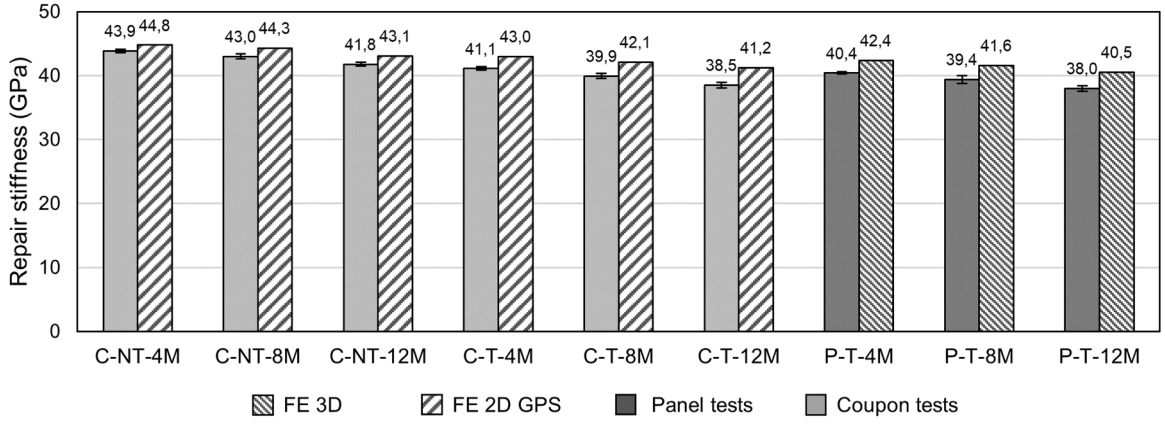

Fig. 24. Effect of step length, damage depth and specimen scale on repair stiffness.

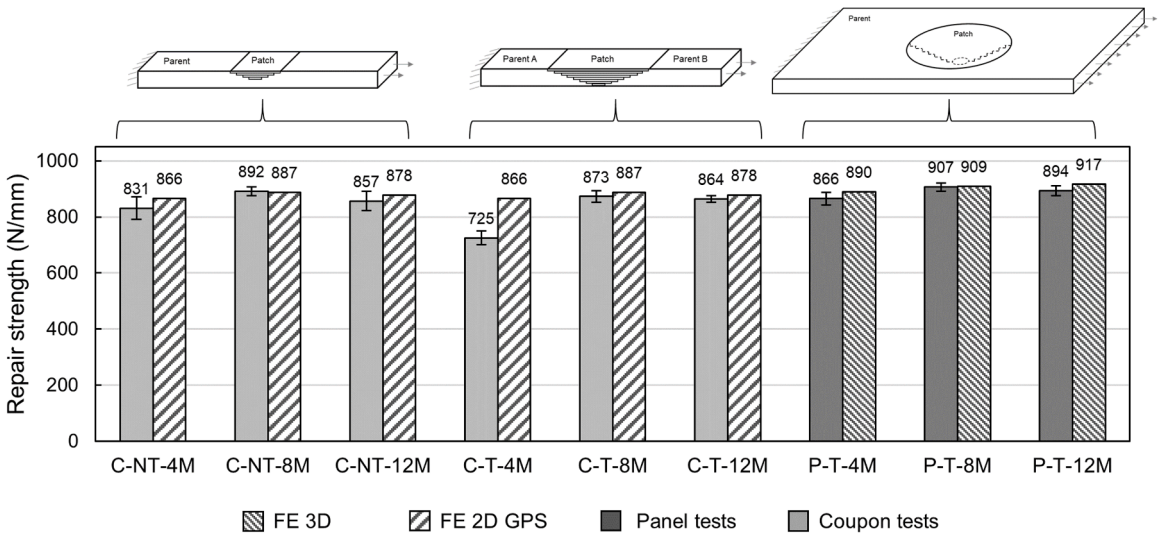

Fig. 25. Effect of step length, damage depth and specimen scale on repair strength.

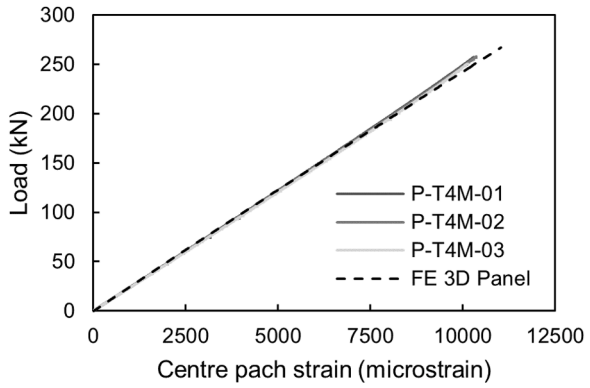

Fig. 26. Strain measured at the centre of the patch of P-T-4M specimens and comparison with FE results.

repaired panel can be written $P = F/b$, where F is the force measured by the load cell and b is the width of the panel, a load by-pass coefficient β can be defined as follows:

$$\beta = 1 - \frac{P_{\text{patch}}}{P} = \left(1 - \frac{E_p \epsilon_p t_p}{F/b}\right) = \left(1 - E_p t_p b \frac{\epsilon_p}{F}\right) \tag{7}$$

With this definition, if β takes positive values, it means that the force flow going through the patch is lower than the mean force flow applied to the specimen. The results obtained for the nine repaired panels are presented in Fig. 27. For through repaired coupons that are equivalent to repaired panels, β will be equal to 0 because the whole load must go through to centre of the patch as there is no other path available. The obtained results for panels should be interpreted very carefully as they rely on the modulus E_p to evaluate the load going through the patch. Indeed, slight error on the value of E_p will significantly change the value of β, but it is reasonable to assume that E_p is the same for all specimens of this study, as they were manufactured with the same material batch. Thus, the variation of β during the tension tests and the deviations between each specimen can be interpreted. First, there is a lack of repeatability and no clear β variation tendency among the P-T-8M specimens, but P-T-4M and P-T-12M specimens do have clearer trends. Indeed, the load bypass tend to increase in P-T-4M specimens as the load increases, while it remains near zero in P-T-12M specimens. The effect becomes clearly visible beyond 200 kN applied, which is about 80 % of the ultimate load. This is compatible with the fact the bonded joint of panels with 4 mm steps is pushed closer to failure than the one of panels

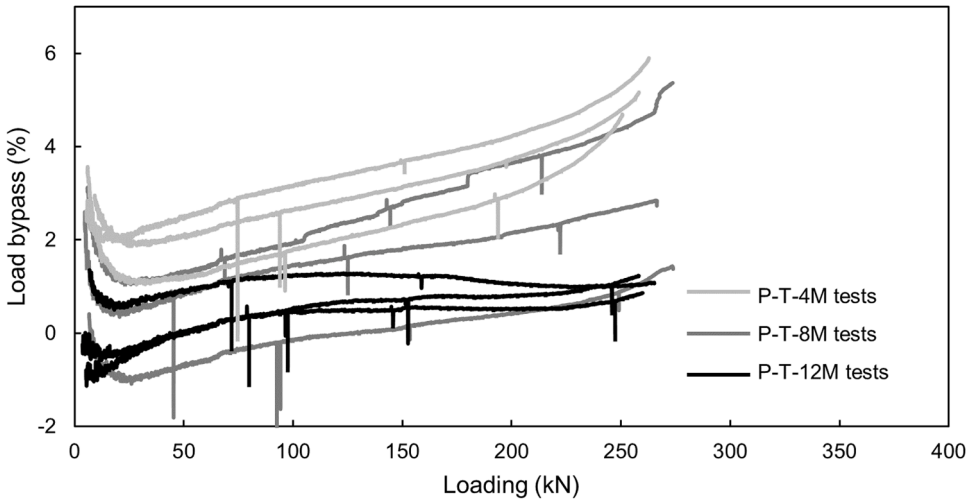

Fig. 27. Load bypass factor computed from stepped repaired panels tension tests.

with 12 mm steps and leads to a higher stress redistribution effect in panels with smaller steps.

5. Conclusions

In this paper, multi-scale testing of CFRP stepped repairs under tension was carried experimentally and numerically, to assess the representativeness of tests at the coupon scale compared to tests at the panel scale. A test matrix with 11 configurations with various including step length, damage depth, patch layup and specimen scale, was proposed to investigate the influence of design parameters and the robustness of the models. FE modelling of stepped repairs in 2D generalized plane strain and 3D was proposed, using CZM and CDM. These models account for damage and delamination in the CFRP laminates, in addition to modelling of the adhesive layer between the parent plate and the repair patch.

Specimens were manufactured by co-bonding with a mobile hot-bonder, as it would be done in situ. Different types of fractures pattern as a function of step length were observed, the main one being neat CFRP laminate fracture in the repaired area. It was shown experimentally that repaired coupons and repaired panel has the local failure mechanisms and the same overall failure locations. Step ends were identified as being the weak spots of the laminates. The failure strength of repaired panels was close to the one of the equivalent repaired coupons unless the step length is in the transition zone between failure of the bondline and failure of the laminates. No increase of strength was found for repairs with 12 mm steps compared to 8 mm steps, indicating that the repairs reach a maximum strength for a given patch layup. Tensions tests on specimens with a patch featuring a matching layup and a 0° overply can achieve almost a 100 % strength recovery rate. This result encourages exploring innovative patch layups in further studies, as the reference overlapping layup may not be the only repair configuration to consider.

FE simulations in 2D and 3D were able to predict the type of failure, including local failure mechanisms, and to predict the failure location compatible with experimental observations. Yet, through repaired coupons with a step length of 4 mm have a mixed fracture pattern that does not appear in FE simulations. A good agreement was found between the repair strength predicted by FE simulations and the strength measured experimentally. The largest strength deviation between tests and FE was of about 16 % the C-T-4M, in all other configurations this deviation is less than 5 %. This conclusion is supported by the agreement in terms of failure scenario between tests and FE results. The larger deviation in the C-T-4M configuration may be related to manufacturing issues. The effective step length may be up to 0.75 mm shorter than the nominal step length, as shown be micrographic observations. The latter is likely to have a stronger impact on the strength of 4mm step repaired coupons compared to the other specimens. The out-of-plane effects that are not captured by the shell elements in FE simulations does not prevent the FE models to predict the specimen's strength accurately. Finally, the assumptions on the balanced nature of the CFRP materials used, and on its compressive behaviour are shown to be acceptable due the correlation between FE and tests results. The modelling methodology proposed here can be qualified as robust, given that all the input properties are directly based on material testing.

These experimental and numerical results extend the conclusions of [30] and [31]. It shows that experimental testing at the scale of a coupon, which is usually proposed in research paper, is indeed suitable to study the behaviour of a whole repaired panel. However, when approaching the step length at which failure happens by patch disbonding, coupons may exhibit an early failure compared to panels. In terms of modelling, 2D FE under generalized plane strain is suitable to predict behaviour of full-scale repaired panels when failure occurs inside the laminates instead of the adhesive layer. It provides a modelling framework that could be further investigated as a less computation-intensive alternative to full 3D models.

Further investigations could be carried-out on the representativeness of a repaired coupon compared to a repaired panel in terms of repair reliability and durability, with the effects of defects, hot-wet aging, impacts and fatigue loading. These issues, which go beyond the simple static strength of a repair, are major concerns and cannot be ignored when designing a composite bonded repair.

CRediT authorship contribution statement

Jean-Baptiste Orsatelli: Writing – original draft, Investigation, Data curation, Conceptualization. **Eric Paroissien:** Writing – review & editing, Validation, Supervision. **Frédéric Lachaud:** Writing – review & editing, Supervision. **Sébastien Schwartz:** Writing – review & editing, Supervision. **Nathalie Barrière:** Writing – review & editing, Resources, Project administration.

Declaration of competing interest

The authors declare that they have no known competing financial interests or personal relationships that could have appeared to influence the work reported in this paper.

Acknowledgements

The authors would like to thank Direction Générale de l'Armement, part of French ministry of Defence, and ISAE-SUPAERO for their financial support.

Data availability

Data will be made available on request.

References

[1] G. Marsh, Composites consolidate in commercial aviation, Reinf. Plast. 60 (5) (2016) 302–305, https://doi.org/10.1016/j.repl.2016.08.002.
[2] T-W Shyr, Y-H. Pan, Impact resistance and damage characteristics of composite laminates, Compos. Struct. 62 (2) (2003) 193–203, https://doi.org/10.1016/S0263-8223(03)00114-4.
[3] RB. Heslehurst, Engineered Repairs of Composite Structures, CRC Press, 2019, https://doi.org/10.1201/9780429198656.
[4] KB Katnam, LFM da Silva, TM. Young, Bonded repair of composite aircraft structures: a review of scientific challenges and opportunities, Prog. Aerosp. Sci. 61 (2013) 26–42, https://doi.org/10.1016/j.paerosci.2013.03.003.
[5] F Erdogan, M. Ratwani, Stress Distribution in Bonded Joints, J. Compos. Mater. 5 (1971) 378–393, https://doi.org/10.1177/002199837100500308.
[6] O. Volkersen, Die Nietkraftverteilung in zugbeanspruchten Nietverbindungen mit konstanten Laschenquerschnitten, Lufsfarhtforschung 15 (1938) 41–47.
[7] LJ. Hart-Smith, Adhesive-bonded scarf and stepped-lap joints. NASA Langley report CR-112237, Douglas Aircraft Co., 1974. https://ntrs.nasa.gov/citations/19740005084.
[8] RDSG Campilho, MFSF de Moura, AMG Pinto, JJL Morais, Domingues JJMS. Modelling the tensile fracture behaviour or CFRP scarf repairs, Compos. Part B 40 (2009) 149–157, https://doi.org/10.1016/j.compositesb.2008.10.008.
[9] RA Odi, CM. Friend, An improved 2D model for bonded composite joints, Int. J. Adhes. Adhes. 24 (5) (2004) 389–405, https://doi.org/10.1016/J.IJADHADH.2001.06.001.
[10] M Ridha, VBC Tan, TE. Tay, Traction–separation laws for progressive failure of bonded scarf repair of composite panel, Compos. Struct. 93 (4) (2011) 1239–1245, https://doi.org/10.1016/j.compstruct.2010.10.015.
[11] H Bendemra, P Compston, PJ. Crothers, Optimisation study of tapered scarf and stepped-lap joints in composite repair patches, Compos. Struct. 130 (2015) 1–8, https://doi.org/10.1016/j.compstruct.2015.04.016.
[12] S Psarras, T Loutas, M Papanaoum, OK Triantopoulos, V. Kostopoulos, Investigating the effect of stepped scarf repair ratio in repair CFRP laminates under compressive loading, J. Compos. Sci. 4 (2020) 153, https://doi.org/10.3390/jcs4040153.
[13] JM Hayes-Griss, AC Orifici, AA Khatibi, An improved progressive failure modelling and damage tolerant design methodology for composite scarf joints with bondline flaws, Compos. Part A 131 (2020) 105776, https://doi.org/10.1016/j.compositesa.2020.105776.
[14] AMG Pinto, RDSG Campilho, MFSF de Moura, IR. Mendes, Numerical evaluation of three-dimensional scarf repairs in carbon-epoxy structures, Int. J. Adhes. Adhes. 30 (5) (2010) 329–337, https://doi.org/10.1016/j.ijadhadh.2009.11.001.

[15] RS Pierce, BG. Falzon, Modelling the size and strength benefits of optimised step/scarf joints and repairs in composite structures, Compos. Part B 173 (2019) 107020, https://doi.org/10.1016/j.compositesb.2019.107020.
[16] S-H Ahn, G. Springer, Repair of composite laminates-II: models, J. Compos. Mater. 32 (11) (1998) 1076–1114, https://doi.org/10.1177/002199839803201103.
[17] CH Wang, AJ. Gunnion, On the design methodology of scarf repairs to composite laminates, Compos. Sci. Technol. 68 (1) (2008) 34–46, https://doi.org/10.1016/J.COMPSCITECH.2007.05.045.
[18] RDSG Campilho, MD Banea, JA Neto, LD. Silva, Modelling adhesive joints with cohesive zone models: effect of the cohesive law shape of the adhesive layer, Int. J. Adhes. Adhes. 44 (2013) 48–56, https://doi.org/10.1016/j.ijadhadh.2013.02.006.
[19] P Liu, J. Zheng, Progressive failure analysis of carbon fiber/epoxy composite laminates using continuum damage mechanics, Mater. Sci. Eng. A 485 (1-2) (2008) 711–717, https://doi.org/10.1016/j.msea.2008.02.023.
[20] S Wang, Z Xie, X. Li, On adhesively bonded stepped-scarf joint: an analytical model and its validation, Mech. Adv. Mater. Struct. 28 (2019) 938–951, https://doi.org/10.1080/15376494.2019.1614699.
[21] JB Orsatelli, E Paroissien, F Lachaud, S. Schwartz, Bonded flush repairs for aerospace composite structures: a review on modelling strategies and application to repairs optimization, reliability and durability, Comp. Struct. 304 (2023) 116338, https://doi.org/10.1016/j.compstruct.2022.116338.
[22] C Xiaoquan, Y Baig, H Renwei, G Yujian, Z. Jikui, Study of tensile failure mechanisms in scarf repaired CFRP laminates, Int. J. Adhes. Adhes. 41 (2013) 177–185, https://doi.org/10.1016/j.ijadhadh.2012.10.015.
[23] TD Breitzman, EV Iarve, BM Cook, GA Schoeppner, RP. Lipton, Optimization of a composite scarf repair patch under tensile loading, Compos. Part A 40 (12) (2009) 1921–1930, https://doi.org/10.1016/j.compositesa.2009.04.033.
[24] Y Baig, X Cheng, HJ Hasham, M Abbas, WA. Khan, Failure mechanisms of scarf-repaired composite laminates under tensile load, J. Braz. Soc. Mech. Sci. Eng. 38 (7) (2015) 2069–2075, https://doi.org/10.1007/s40430-015-0460-z.
[25] FH Darwish, KN. Shivakumar, Experimental and analytical modeling of scarf repaired composite panels, Mech. Adv. Mater. Struct. 21 (3) (2013) 207–212, https://doi.org/10.1080/15376494.2013.834096.
[26] HM Chong, SL Liu, AS Subramanian, SP Ng, SW Tay, SQ Wang, S. Feih, Out-of-autoclave scarf repair of interlayer toughened carbon fibre composites using double vacuum debulking of patch, Compos. Part A 107 (2018) 224–234, https://doi.org/10.1016/j.compositesa.2018.01.001.
[27] C Soutis, FZ. Hu, Failure analysis of scarf-patch-repaired carbon fiber/epoxy laminates under compression, AIAa J. 38 (4) (2000) 737–740, https://doi.org/10.2514/2.1027.
[28] AJ Gunnion, I. Herszberg, Parametric study of scarf joints in composite structures, Compos. Struct. 75 (1) (2006) 364–376, https://doi.org/10.1016/j.compstruct.2006.04.053.
[29] B Liu, F Xu, W Feng, R Yan, W Xie, Experiment and design methods of composite scarf repair for primary-load bearing structures, Compos. Part A 88 (2016) 27–38, https://doi.org/10.1016/j.compositesa.2016.05.011.
[30] S Tashi, A. Abedian, A comprehensive 2 Dimensional and 3 Dimensional FE study of scarf repair for a variety of common composite laminates under in-plane uniaxial and equibiaxial loadings, Int. J. Adhes. Adhes. 114 (2022) 103092, https://doi.org/10.1016/j.ijadhadh.2022.103092.
[31] JB Orsatelli, P Paroissien, F Lachaud, S. Schwartz, Influence on modelling hypotheses on strength assessment of CFRP stepped repairs, Int. J. Adhes. Adhes. 132 (2024) 103682, https://doi.org/10.1016/j.ijadhadh.2024.103682.
[32] X Han, M Hu, Y Wang, B Liu, LFM da Silva, X. Guo, Experiments and modelling of competitive failure behaviour of CFRP stepped-lap repairs with different design parameters, Thin. Walled Struct. 199 (2024) 111836, https://doi.org/10.1016/j.tws.2024.111836.
[33] M Damghani, GA Atkison, P Thapa, J Joy, M Monaghan, P Maleki, C. Ward, An experimental investigation of tensile residual strength of repaired composite laminates after low velocity impact, Thin. Walled Struct. 200 (2024) 111896, https://doi.org/10.1016/j.tws.2024.111896.
[34] W Xiao, G Sha, X Lu, H Zuo, M Cao, R Soman, W Ostachowicz, Experimental and numerical studies on compressive failure behaviors of stepped-scarf repaired composite stiffened panels, Eng. Fail. Anal. 163 (2024) 108458, https://doi.org/10.1016/j.engfailanal.2024.108458.
[35] S Psarras, T Loutas, G Sotiriadis, V. Kostopoulos, Evaluating the compressive strength of stepped scarf repaired single stiffener composite panels, J. Comp. Mater. 57 (18) (2023) 2887–2898, https://doi.org/10.1177/00219983231178684.
[36] A Riccio, A Sellitto, A Garofano, G Ingenito, M. Zarrelli, Numerical-experimental study on the compressive behaviour of repaired composite panels, J. Comp. Part. B 251 (2023) 110446, https://doi.org/10.1016/j.compositesb.2022.110466.
[37] Xiao W, Sha G, Lu, X, Zuo H, Cao M, Ostachowicz W. Compressive failure analysis of composite honeycomb sandwich panels with impact damage and stepped-scarf repairs Thin Walled Struct 2024;201:112012 https://doi.org/10.1016/j.tws.2024.112012.
[38] M Damghani, J Bakunowicz, A. Murphy, Understanding the influence of laminate stacking sequence on strain/stress concentrations in thin laminates at repair holes with large scarf angles, J. Compos. Mater. 53 (28–30) (2019) 4273–4284, https://doi.org/10.1177/0021998319855772.
[39] F Collombet, Y Davila, S Avila, A Morales, L Crouzeix, Y-H Grunevald, et al., Proof of a composite repair concept for aeronautical structures: a simplified method, Mech. Ind. 20 (8) (2019) 812, https://doi.org/10.1051/meca/2020056.
[40] Dassault Systèmes, ABAQUS 2016 Analysis User's Guide: 32.5.1 Defining the Constitutive Response of Cohesive Elements Using a Traction-separation Description, Abaqus, 2016.
[41] Dassault Systèmes, ABAQUS 2016 Analysis User's Guide: 24.3 Damage and Failure for Fiber-Reinforced Composites, Abaqus, 2016.
[42] HEXCEL, HexPlyM18/1 180 Degree Celcius Curing Epoxy Matrix Product Data, HEXCEL, Stamford CT, USAE, 2011.
[43] HEXCEL, HexBond 312 Modified Epoxy Film Adhesive Product Data Sheet, HEXCEL, Stamford CT, USAE, 2019.
[44] A Deheeger, JD Mathias, M Grédiac, V. Verney, Studying the thermoviscoelastic response of the Redux 312 adhesive. Part 1: experimental characterization, Int. J. Adhes. Adhes. 31 (2) (2011) 68–74, https://doi.org/10.1016/j.ijadhadh.2010.11.008.
[45] A Deheeger, JD Mathias, M. Grédiac, Studying the thermoviscoelastic response of the Redux 312 adhesive. Part 2: Modeling, Int. J. Adhes. Adhes. 31 (2) (2011) 57–67, https://doi.org/10.1016/j.ijadhadh.2010.11.009.
[46] A Turon, CG Davila, PP Camanho, J. Costa, An engineering solution for mesh size effects in the simulation of delamination using cohesive zone models, Eng. Frach. Mech. 74 (2007) 1665–1682, https://doi.org/10.1016/j.engfracmech.2006.08.025.
[47] TPZ Marques, S Mayer, GM Candido, MC. Rezende, Fractographic analysis of scarf repaired carbon/epoxy laminates submitted to tensile strength, Eng. Fail. Anal. 124 (2021) 105374, https://doi.org/10.1016/j.engfailanal.2021.105374.